AGU PUBLICATIONS

JGR

Journal of Geophysical Research: Atmospheres

RESEARCH ARTICLE
10.1002/2016JD026370

Key Points:
- A simple temperature domain two-source energy balance model has been developed
- This model produced comparable accuracy when compared with two other models
- This model provides an alternative method for mapping field surface heat fluxes

Supporting Information:
- Supporting Information S1

Correspondence to:
Y. Yao,
boyyunjun@163.com

Citation:
Yao, Y., et al. (2017), A simple temperature domain two-source model for estimating agricultural field surface energy fluxes from Landsat images, *J. Geophys. Res. Atmos.*, *122*, 5211-5236, doi:10.1002/2016JD026370.

Received 12 DEC 2016
Accepted 22 APR 2017
Accepted article online 26 APR 2017
Published online 27 MAY 2017

A simple temperature domain two-source model for estimating agricultural field surface energy fluxes from Landsat images

Yunjun Yao[1], Shunlin Liang[1], Jian Yu[1], Jiquan Chen[2], Shaomin Liu[3], Yi Lin[4], Joshua B. Fisher[5], Tim R. McVicar[6], Jie Cheng[1], Kun Jia[1], Xiaotong Zhang[1], Xianhong Xie[1], Bo Jiang[1], and Liang Sun[7]

[1]State Key Laboratory of Remote Sensing Science, Institute of Remote Sensing Science and Engineering, Faculty of Geographical Science, Beijing Normal University, Beijing, China, [2]CGCEO/Geography, Michigan State University, East Lansing, Michigan, USA, [3]State Key Laboratory of Earth Surface Processes and Resource Ecology, School of Natural Resources, Faculty of Geographical Science, Beijing Normal University, Beijing, China, [4]Institute of Remote Sensing and GIS, Peking University, Beijing, China, [5]Jet Propulsion Laboratory, California Institute of Technology, Pasadena, California, USA, [6]CSIRO Land and Water, Canberra, ACT, Australia, [7]USDA-ARS Hydrology and Remote Sensing Laboratory, Beltsville, Maryland, USA

Abstract A simple and robust satellite-based method for estimating agricultural field to regional surface energy fluxes at a high spatial resolution is important for many applications. We developed a simple temperature domain two-source energy balance (TD-TSEB) model within a hybrid two-source model scheme by coupling "layer" and "patch" models to estimate surface heat fluxes from Landsat thematic mapper/Enhanced Thematic Mapper Plus (TM/ETM+) imagery. For estimating latent heat flux (LE) of full soil, we proposed a temperature domain residual of the energy balance equation based on a simplified framework of total aerodynamic resistances, which provides a key link between thermal satellite temperature and subsurface moisture status. Additionally, we used a modified Priestley-Taylor model for estimating LE of full vegetation. The proposed method was applied to TM/ETM+ imagery and was validated using the ground-measured data at five crop eddy-covariance tower sites in China. The results show that TD-TSEB yielded root-mean-square-error values between 24.9 (8.9) and 78.2 (21.4) W/m^2 and squared correlation coefficient (R^2) values between 0.60 (0.51) and 0.97 (0.90), for the estimated instantaneous (daily) surface net radiation, soil, latent, and sensible heat fluxes at all five sites. The TD-TSEB model shows good accuracy for partitioning LE into soil (LE_{soil}) and canopy (LE_{canopy}) components with an average bias of 11.1% for the estimated LE_{soil}/LE ratio at the Daman site. Importantly, the TD-TSEB model produced comparable accuracy but requires fewer forcing data (i.e., no wind speed and roughness length are needed) when compared with two other widely used surface energy balance models. Sensitivity analyses demonstrated that this accurate operational model provides an alternative method for mapping field surface heat fluxes with satisfactory performance.

1. Introduction

Accurate estimation of agricultural surface energy fluxes at high spatial resolution is essential for monitoring crop water stress, irrigation scheduling, and water resource management [*Anderson et al.*, 1997; *Liang et al.*, 2010; *McVicar and Jupp*, 2002; *Norman et al.*, 1995; *Yang et al.*, 2013; *Yao et al.*, 2015]. Although direct ground measurements of surface energy fluxes from eddy-covariance (EC) flux tower observations can provide representative values of latent heat flux (LE) and sensible heat flux (*H*) at scales of several decades and hundreds of meters [*Choi et al.*, 2009; *Fisher et al.*, 2008; *Jung et al.*, 2010; *Liu et al.*, 2011; *Tang et al.*, 2010], the spatial isolation and high costs of these direct measurements restrict their application for characterizing spatiotemporal LE and *H* patterns over regional (i.e., >20,000 km^2) agricultural zones. Therefore, there is an urgent demand for an economically feasible means of accurately estimating and mapping regional-scale LE at relatively high spatial resolution, acknowledging farmer management practices.

Land surface temperature (LST) derived from high spatial resolution thermal satellite data, such as the Landsat thematic mapper/Enhanced Thematic Mapper Plus (TM/ETM+), has been widely used to drive agricultural LE models for partitioning available energy in LE and *H* [*Norman et al.*, 1995; *Kustas and Norman*, 1999; *Allen et al.*, 2007; *Wang and Dickinson*, 2012; *McVicar and Jupp*, 1999]. Satellite-based one-source energy balance (OSEB) models generally use LST as a surrogate for aerodynamic temperature (T_{ao}) to calculate *H*,

and then LE is calculated as the residual of the surface energy budget [*Bastiaanssen et al.*, 1998]. Examples of widely used OSEB models include Surface Energy Balance Algorithm for Land algorithm [*Bastiaanssen et al.*, 1998], Surface Energy Balance System [*Su*, 2002], Three-Temperature (3T) model [*Qiu et al.*, 2006], and Satellite-Based Energy Balance for Mapping Evapotranspiration with Internalized Calibration (METRIC) [*Allen et al.*, 2007]; to reduce the errors in H and LE estimation by using spatial contextual information of LST to replace the conventional gradients of surface temperature and air temperature (LST-T_a), these OSEB models treat vegetation and soil as one "big leaf" with uniform temperature and aerodynamic resistance for heat transfer at the same height. This approach yields significant biases when applied to partially vegetated landscapes [*Kalma et al.*, 2008; *Verhoef et al.*, 1997].

To deal with this problem in the OSEB models, satellite-based two-source energy balance (TSEB) models partition the LE and H fluxes into soil evaporation and vegetation transpiration components and yield more reliable flux estimates than do OSEB models over heterogeneous surfaces with sparse vegetation cover [*Norman et al.*, 1995; *Sánchez et al.*, 2008; *Song et al.*, 2016; *C. Yang et al.*, 2015]. An original model was proposed by *Norman et al.* [1995] with subsequent improvements developed by many scholars [*Kustas and Norman*, 1997; *Kustas et al.*, 1998; *Anderson et al.*, 1997; *Sánchez et al.*, 2008; *Song et al.*, 2016; *Yang and Shang*, 2013]. Similar to the OSEB models, TSEB models are still sensitive to their use of the temperature differences to estimate H. To overcome this problem, two different modeling schemes: (i) methods using the temporal variation of LST [*Anderson et al.*, 1997, 2008; *Nishida et al.*, 2003; *Norman et al.*, 2000, 2003] and (ii) methods using the spatial variation of LST [*Long and Singh*, 2012; *Yang and Shang*, 2013; *Zhang et al.*, 2005], have been developed and improved to reduce the flux estimation errors. Overviews of these modeling schemes since the 1990s are summarized in Table 1, including their main advantages and limitations. However, there are two problems when using these TSEB models that have not yet been fully solved. First, a longstanding limitation associated with most TSEB models is that aerodynamic resistances and excess resistances to heat exchange are usually calculated based on the local data for surface roughness length and wind-profile measurements that cannot be readily retrieved from satellite data [*Kalma et al.*, 2008; *Nishida et al.*, 2003; *Seguin and Itier*, 1983; *Zhang et al.*, 2005]. Given that area averaging of both roughness length and wind speed (u) is highly nonlinear [*Boegh et al.*, 2002; *Kalma et al.*, 2008], inaccurate point-based footprint representation at the pixel scale may unavoidably lead to different results and uncertainties. Second, complex parameterization schemes and accumulated errors from too many input variables also magnify biases in H and LE estimations [*Dolman*, 1993; *Ershadi et al.*, 2014; *Long and Singh*, 2012; *Norman et al.*, 1995; *Zhang et al.*, 2005]. Although some spatial contextual models based on vegetation index (VI) and LST space minimize the influence of u, such spatial contextual models are not operational if the area of interest does not include a full range of land surface types and conditions [*Nishida et al.*, 2003; *Long and Singh*, 2012; *Yang and Shang*, 2013].

To overcome these two problems, it is important to design an operational TSEB model based on a simplified framework of total aerodynamic resistances to avoid using both roughness length and u as inputs. In this study, a simple operational hybrid two-source model is developed to achieve this goal. This paper has three main objectives: (i) to describe this hybrid temperature domain two-source model, which couples the residual of the energy balance equation and a modified Priestley-Taylor (PT) model for estimating agricultural field surface energy fluxes; (ii) to evaluate this simple two-source model using the EC tower and the corresponding Landsat TM/ETM+ imagery collected from five cropland sites across northern China; and (iii) to perform a case study of mapping agricultural field surface fluxes using Landsat TM/ETM+ imagery.

2. Methods

2.1. The Temperature Domain Two-Source Model

The temperature domain two-source energy balance (TD-TSEB) model developed in this study includes three modules: (i) a hybrid two-source model framework that couples the TSEB layer and patch models, (ii) a temperature domain model for LE_s estimation, and (iii) a PT model for LE of full canopy (LE_c) estimation. These three modules are introduced in turn the following sections.

2.1.1. Hybrid Two-Source Model Framework

In our model, a TSEB layer model is used to partition net radiation (R_n) between the canopy and the soil surface based on the Beer-Lambert law (Figure 1) [*Ruimy et al.*, 1999]:

Table 1. Summary of Relevant Two-Source Models Using Thermal Remote Sensing Data (the Current Paper Is Added for Completeness)

Study	Model Name	Modeling Scheme	Validation Data	Model Performance	Main Advantages	Main Disadvantages
1. *Norman et al.* [1995]	Original two-source model (TSEB)	The Priestley-Taylor iteration approach	Monsoon 1990; *FIFE*	RMSE: 35–60 W/m^2 for *G*, *H*, and LE	Wide applicability due to the uses of the directional brightness temperatures	1. High sensitive to errors of T_s and T_a; 2. Requires *u* to calculate resistance and *u* is not available from satellite data
2. *Kustas and Norman* [1997]	TSEB using T_s at two view angles	Use of T_s observations at two different angles	*FIFE*	25–40% errors for LE	Does not require f_v and Priestley-Taylor model	1. Requires T_s at two view angles; 2. Requires *u* to calculate resistance
3. *Anderson et al.* [1997]	A two-source time- integrated model	Use of temporal changes in T_s rather than absolute T_s	*FIFE*	RMSE: less than 50 W/m^2 for LE	1. Reduced sensitivity to absolute T_s-T_a Differences; 2. No observation of T_a required	1. Requires early morning sounding for determining inversion lapse rate; 2. Requires *u* to calculate resistance
4. *Kustas et al.* [1998]	A revised TSEB model	Use of near-surface moisture from a passive microwave sensor	Monsoon 1990	20–30%errorsfor LE	1. Reduced the errors in LE estimates using soil moisture to replace T_s; 2. Minor effect of R_s on daytime LE	1. Requires soil moisture from microwave remote sensing data; 2. Requires *u* to calculate resistance
5. *Norman et al.* [2000]	TSEB model using Dual-Temperature Difference	Use of time rate of change in T_s and T_a	Monsoon 1990; *SGP*97	Differences of more than 50 W/m^2 for LE	Requires minimal ground-based data and does not require modeling boundary layer development	Requires nonlocal *u* to calculate resistance
6. *Norman et al.* [2003]	TSEB model coupled to Disaggregated Atmosphere-Land Exchange Inverse	Use of temporal changes in geostationary T_s	*SGP*97	RMSE: 40 W/m^2 for LE	Useful to estimate surface fluxes on the 10^1–10^2 m scale	Requires low and high-resolution satellite data
7. *Nishida et al.* [2003]	A linear two-source model	The vegetation index (VI)-surface temperature diagram	AmeriFlux	Standard error: 24.01–85.91 W/m^2 for daytime LE	1. Low sensitivity to errors of T_s; 2. It's easy to operate	1. Relationship between LE and T_s complicated with temperature control on LE; 2. Requires *u* to calculate resistance for determining the highest T_s
8. *Zhang et al.* [2005]	Pixel component arranging and comparing algorithm	The theoretical boundary condition is accurately determined in the f_v-surface temperature space	Yucheng; Dongping lake	Reasonable accuracy for LE estimation	1. Low sensitivity to errors of T_s; 2. Requires few meteorological variables for LE estimation	1. The area of interest needs a full range of land surface types and conditions; 2. Requires *u* to determine temperatures the theoretical boundary
9. *Anderson et al.* [2008]	TSEB coupled to the light-use efficiency model	LUE model to replace PT model for estimating vegetation transpiration	*SGP*97	RMSE: 34 W/m^2 for LE	Improve the accuracy of LE estimates in comparison to the TSEB-PT model	Requires many input parameters, such as, *u*, the ambient vapor pressure and CO_2 concentration
10. *Sánchez et al.* [2008]	A simplified TSEB model (STSEB)	The Ohm's law-type equation to replace the PT model	*USDA-ARS*: corn	RMSE: 15–50 W/m^2 for LE	It is a simplified version of the TSEB model and is easy to operate	1. Sensitive to errors of T_s and T_a; 2. Requires *u* to calculate resistance

Table 1. (continued)

Study	Model Name	Modeling Scheme	Validation Data	Model Performance	Main Advantages	Main Disadvantages
11. *Long and Singh* [2012]	A two-source trapezoid model	The temperature decomposition method is developed by interpreting the f_v - surface temperature trapezoid space	*SMACEX*	RMSE: 45.6 W/m^2 for LE estimation using TM/ETM+ data	1. Reduces uncertainties arising from the specification of warm and cold edges/pixels involved in one-source models; 2. It is unique in applying a two-source scheme to the trapezoidal framework of the f_v-surface temperature space	1. The theoretical boundary conditions necessitates homogeneous meteorological conditions; 2. Ignores the effects of advection on partitioning of turbulent energy fluxes; 3. Requires u to calculate resistance for determining the theoretical boundary
12. *Yang and Shang* [2013]	A hybrid dual-source scheme and trapezoid framework–based model (HTEM)	Combines the layer approach and patch approach based on the VI-surface temperature trapezoidal space	*SMACEX*	Errors in 6.4% for LE estimation	1. The extreme boundaries were determined theoretically in its trapezoid Framework; 2. Allows the trapezoid model to consider the surface aerodynamic characteristics	1. The most sensitive to temperature variables; 2. Ignores the effects of advection on partitioning of turbulent energy fluxes; 3. Requires u to calculate resistance
13. This study	A simple temperature domain two-source model (TD-TSEB)	A temperature domain residual of the energy balance equation	Haihe; HiWATER-MUSOEXE	RMSE: 24.9–77.3 W/m^2 for R_n, G, LE and H	1. Requires few inputs and avoids requiring u to estimate surface fluxes; 2. Overcomes the complicated parameterization of resistance	1. Moderate sensitive to errors of T_s and T_a; 2. Ignores the effects of advection on partitioning of turbulent energy fluxes

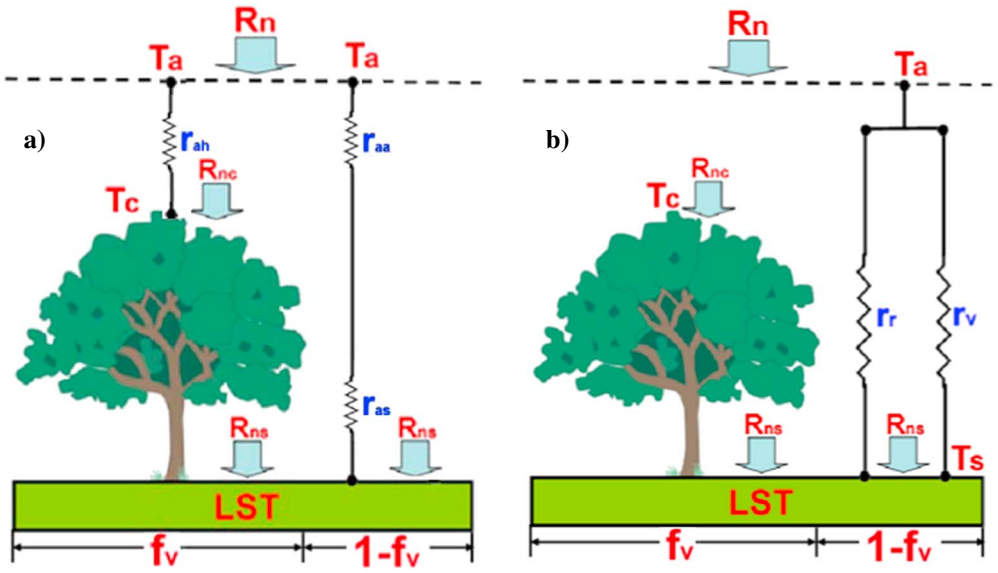

Figure 1. Schematic diagrams of (a) the traditional TSEB model [*Sánchez et al.*, 2008; *Yang and Shang*, 2013] and (b) the temperature domain TSEB model developed here. r_{ah} refers to the aerodynamic resistance to heat transfer between the canopy and the reference height. The other symbols are defined in section 2.1.

$$R_{ns} = R_n \exp(-k_{ns} LAI) \text{ and} \tag{1}$$

$$R_{nc} = R_n - R_{ns}, \tag{2}$$

where R_{ns} and R_{nc} are the total net surface radiation partitioned to the soil and canopy respectively, in W/m^2, and k_{ns} is an extinction coefficient (0.6; unitless) [*Impens and Lemur*, 1969]. The leaf area index (LAI) is estimated using a simple statistical method driven by the fractional vegetation coverage (f_v) [*Ross*, 1976].

$$\text{LAI} = -\frac{1}{k_{par}} \ln(1 - f_v) \text{ and} \tag{3}$$

$$f_v = \frac{\text{NDVI} - \text{NDVI}_{\text{min}}}{\text{NDVI}_{\text{max}} - \text{NDVI}_{\text{min}}}, \tag{4}$$

where k_{par} is an empirical coefficient (0.5; unitless) [*Ross*, 1976]. NDVI_{min} and NDVI_{max} are the minimum and maximum normalized difference vegetation index (NDVI) during the study period, which are set as invariant constants: 0.05 and 0.85, respectively [*Carlson and Ripley*, 1997]. The f_v represents the variations in vegetation state and canopy conductance response to changes in environmental factors such as the plant moisture stress, vapor pressure deficit, fractional absorbed photosynthetically active radiation, and atmospheric CO_2 concentration [*Tucker*, 1979; *Donohue et al.*, 2013].

A TSEB patch model is then used to partition R_n into LE, H, and soil heat flux (G). The LE and H of each component (soil or canopy) in W/m^2 is estimated as the average value per unit of ground area weighted according to the fractional coverage of each component [*Yang and Shang*, 2013]:

$$R_{nc} = f_v \times (\text{LE}_c + H_c) \text{ and} \tag{5}$$

$$R_{ns} - G = (1 - f_v) \times (\text{LE}_s + H_s), \tag{6}$$

where H_c and H_s are the sensible heat flux of the canopy and soil, respectively, in W/m^2. G (W/m^2) is calculated using a semiempirical algorithm provided by *Choudhury et al.* [1987]:

$$G = a_k R_{ns}, \tag{7}$$

where a_k is an empirical coefficient and is set as 0.31 herein [*Anderson et al.*, 1997], though it varies from 0.12 to 0.5 acquired from measurements of above-canopy net radiation and soil heat flux at midday [*Choudhury et al.*, 1987; *Kustas et al.*, 1998]. According to the theoretical basis of the patch model [*Lhomme and Chehbouni*, 1999], the total LE can be expressed as

$$\text{LE} = f_v \times \text{LE}_c + (1 - f_v) \times \text{LE}_s. \tag{8}$$

2.1.2. Temperature Domain Model for LE_s Estimation

A residual method based on the surface energy budget used to estimate LE_s and H_s is calculated using the following Ohm's law-type equation:

$$H_s = \frac{\rho C_p (T_s - T_a)}{r_{\text{atot}}}, \tag{9}$$

where ρ is the air density (kg/m^3), C_p is the specific heat of air at constant pressure (J/kg/K), T_s is the soil surface temperature (°C), T_a is the air temperature (°C), and r_{atot} is the total aerodynamic resistance to vapor transport at the soil surface (s/m).

The r_{atot} (s/m) term is usually estimated using *Thom* [1975] driven by u, surface roughness length, and atmospheric stability conditions. *Stewart et al.* [1994] and *Kustas et al.* [2003] computed r_{atot} as the sum of r_{aa} (s/m) and r_{ex} (s/m). where r_{aa} is the aerodynamic resistance to sensible heat transfer between the point $Z_{om} + d$ (Z_{om}: canopy roughness length for momentum (m), d: displacement height (m)) and the reference height, and r_{ex} is the excess resistance, which characterizes the difference between the momentum and sensible heat transfer. Similarly *Sánchez et al.* [2008] defined r_{atot} as the sum of r_{aa} and the aerodynamic resistance (r_{as}) to heat flow in the boundary layer immediately above the soil surface (Figure 1a). Here r_{atot} is parallel to both the radiative heat transfer resistance (r_r (s/m)) [*Choudhury and DiGirolamo*, 1998; *Mu et al.*, 2007; *Zhang et al.*, 2010] and the convective heat transfer resistance (r_v (s/m)) [*Choudhury and Monteith*, 1988; *Kondo*, 2000; *Sauer et al.*, 1995; *Stewart et al.*, 1994], namely (Figure 1b):

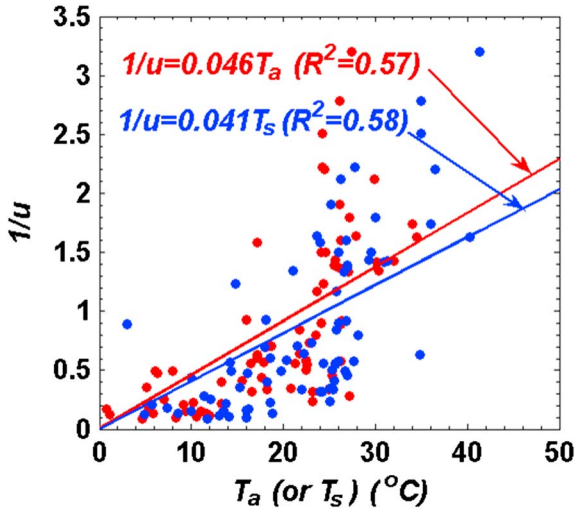

Figure 2. An example of the scatterplot of the instantaneous temperature (T_a or T_s) and 1/u from five EC tower sites of China.

$$\frac{1}{r_{\text{atot}}} = \frac{1}{r_r} + \frac{1}{r_v}, \tag{10}$$

$$r_r = \frac{\rho C_p}{4\varepsilon_s \delta (T_a + 273.15)^3}, \text{and} \tag{11}$$

$$r_v = \frac{k_r}{u}, \tag{12}$$

where ε_s is the bare soil surface emissivity (0.96), δ is the Stefan-Boltzman constant ($5.67 \times 10^{-8} \text{Wm}^{-2}\,\text{K}^{-4}$), and k_r is a unitless empirical coefficient. Previous studies have shown that temperature (namely, T_a and LST) and u variability play opposing roles in flux estimation [*Bertoldi et al.*, 2007] because temperature affects atmospheric pressure, which in turn affects the u. Therefore, some scientists have replaced u with T_a to optimize r_v [*Wallace and Holwill*, 1997; *Jones*, 1992; *Mu et al.*, 2007; *Mu et al.*, 2011; *Zhang et al.*, 2009]. We used a simple positive proportional equation of temperature to parameterize r_v because of the good correlation between instantaneous temperature (T_a or T_s) and 1/u [*Zhang et al.*, 2013], with an example shown in Figure 2 ($R^2 > 0.55$). Thus, equation (12) can be expressed as

$$r_v = k_{ua} T_a = k_{us} T_s, \tag{13}$$

where both k_{ua} and k_{us} are unitless empirical coefficients. By combining equations (6), (9), (10), (11), and (13), we obtain the following formula for LE_s:

$$\text{LE}_s = \frac{R_{ns} - G}{1 - f_v} - 4\varepsilon_s \delta (T_a + 273.15)^3 (T_s - T_a) - \frac{\rho C_p}{k_{us} - k_{ua}}. \tag{14}$$

In practice, T_s is a synthetic thermodynamic factor of the complex radiative and convective interactions associated with radiation, heat, and water exchange across the land surface [*Liu et al.*, 2012]. Therefore, equation (14) is considered a continuous function of T_s because T_s is a key state variable of LE_s, and LE_s varies in a given temperature domain. When T_s reaches equilibrium temperature (T_0, $T_0 = T_a$) [*World Meteorological Organization*, 2008; *Edinger et al.*, 1968], which is defined as the surface temperature of the evaporating surface at which the net rate of heat exchange (by shortwave and longwave radiation, and conduction and evaporation) is zero, LE_s will reach equilibrium evaporation (LE_e). Thus, equation (14) can be expressed as

$$\text{LE}_e = \frac{R_{ns0} - G_0}{1 - f_v} - \frac{\rho C_p}{k_{us} - k_{ua}}, \tag{15}$$

where R_{ns0} is the net radiation partitioned to the soil if $T_s = T_0$ and G_0 is the soil heat flux if $T_s = T_0$. Based on the definition of LE_e, i.e., the evaporation under conditions of zero advection and no boundary layer growth when

the air above a free water surface of a large spatial scale becomes saturated [*Eichinger et al.*, 1996; *Kim and Entekhabi*, 1997], LE_e is calculated as

$$LE_e = \frac{\Delta}{\Delta+\gamma}\frac{R_{ns0}-G_0}{1-f_v}. \tag{16}$$

By combining equations (14), (15), and (16) (Text S1 in the supporting information), we obtain

$$LE_s = \frac{\Delta}{\Delta+\gamma}\frac{R_{ns}-G}{1-f_v} - 4\varepsilon_s\delta\left[\frac{\gamma}{\Delta+\gamma}(1-a_k)(1-f_v)^{k_{ns}/k_{par}}+1\right](T_a+273.15)^3(T_s-T_a). \tag{17}$$

2.1.3. Priestley-Taylor Model for LE_c Estimation

A modified Priestley-Taylor (PT) model is used to estimate LE_c [*Norman et al.*, 1995; *Fisher et al.*, 2008; *Yao et al.*, 2013]. Based on the equation (5) and the PT equation, the model for vegetation transpiration is expressed as

$$LE_c = \alpha f_v f_T \frac{\Delta}{\Delta+\gamma}\frac{R_{nc}}{f_v} = \alpha f_T \frac{\Delta}{\Delta+\gamma}R_{nc} \text{ and} \tag{18}$$

$$f_T = \exp\left[-\left(\frac{T_a-T_{\text{opt}}}{T_{\text{opt}}}\right)^2\right], \tag{19}$$

where a is the PT coefficient (1.26) and f_T is the temperature constraint, with an optimum air temperature (T_{opt}) set at 25°C [*Potter et al.*, 1993; *Fisher et al.*, 2008; *Yao et al.*, 2013; *Yuan et al.*, 2010]. Considering that f_v reflects the biophysical capacity for energy acquisition by the canopy and it decreases in response to plant and soil moisture stress, we directly consider f_v as a moisture constraint to avoid soil moisture as input though there is a time lag between soil moisture and NDVI changes [*Chen et al.*, 2016; *Fisher et al.*, 2008; *Norman et al.*, 1995; *Yao et al.*, 2013]. Inputs, intermediate variables, outputs, and computation procedures of TD-TSEB are summarized in Figure 3.

2.2. Daily LE Computation

Because remotely sensed LE values are instantaneous observations that not representative of an entire day, an extrapolation approach is required. A common method for extrapolating daily (24 h period) totals from instantaneous satellite-based LE estimates is to assume a constant evaporative fraction (EF), which is the ratio of LE to available energy (R_n-G) [*Nishida et al.*, 2003; *Sugita and Brutsaert*, 1991]. In general, EF is nearly constant during the midday hours for a given day, and a single observation at a given time of day can be used to estimate the daily LE [*Lhomme and Elguero*, 1999]. However, previous studies have showed that midday EF using the EC tower data to estimate daily total flux results in underestimating the observed totals by 5–10% [*Anderson et al.*, 2007; *Brutsaert and Sugita*, 1992; *Van Niel et al.*, 2011]. We used this invariant EF method to estimated daily LE and revised the calculation of daily EF as

$$EF_{\text{daily}} = 1.1EF_{\text{ins}} = 1.1\frac{LE_{\text{ins}}}{R_{\text{nins}}-G_{\text{ins}}} \text{ and} \tag{20}$$

$$LE_{\text{daily}} = EF_{\text{daily}} \times \left(R_{\text{ndaily}} - G_{\text{daily}}\right), \tag{21}$$

where EF_{daily} (unitless) is the daytime evaporation fraction, EF_{ins} (unitless) is the instantaneous midday evaporation fraction, and LE_{ins} (W/m^2) is the instantaneous midday latent heat flux. R_{nins} (W/m^2) and G_{ins} (W/m^2) are the instantaneous midday net radiation and soil heat flux, respectively, and R_{ndaily} (W/m^2) and G_{daily} (W/m^2) are the daily net radiation and soil heat flux, respectively.

2.3. Sensitivity Analysis Method

To examine the contributions of forcing variables to the TD-TSEB model output, sensitivity analysis of the major variables of the TD-TSEB model was performed using a simple relative sensitivity method suggested by *Zhan et al.* [1996]. In this method, sensitivity to each input variable (incident surface solar radiation, albedo, NDVI, LST, and T_a) is calculated by comparing the estimated LE (LE_0) using the reference inputs with LE values estimated through varying the input variable v. The sensitivity coefficient (S_v) can be expressed as

$$S_v = \frac{LE_{v\pm} - LE_0}{LE_0} \times 100\%. \tag{22}$$

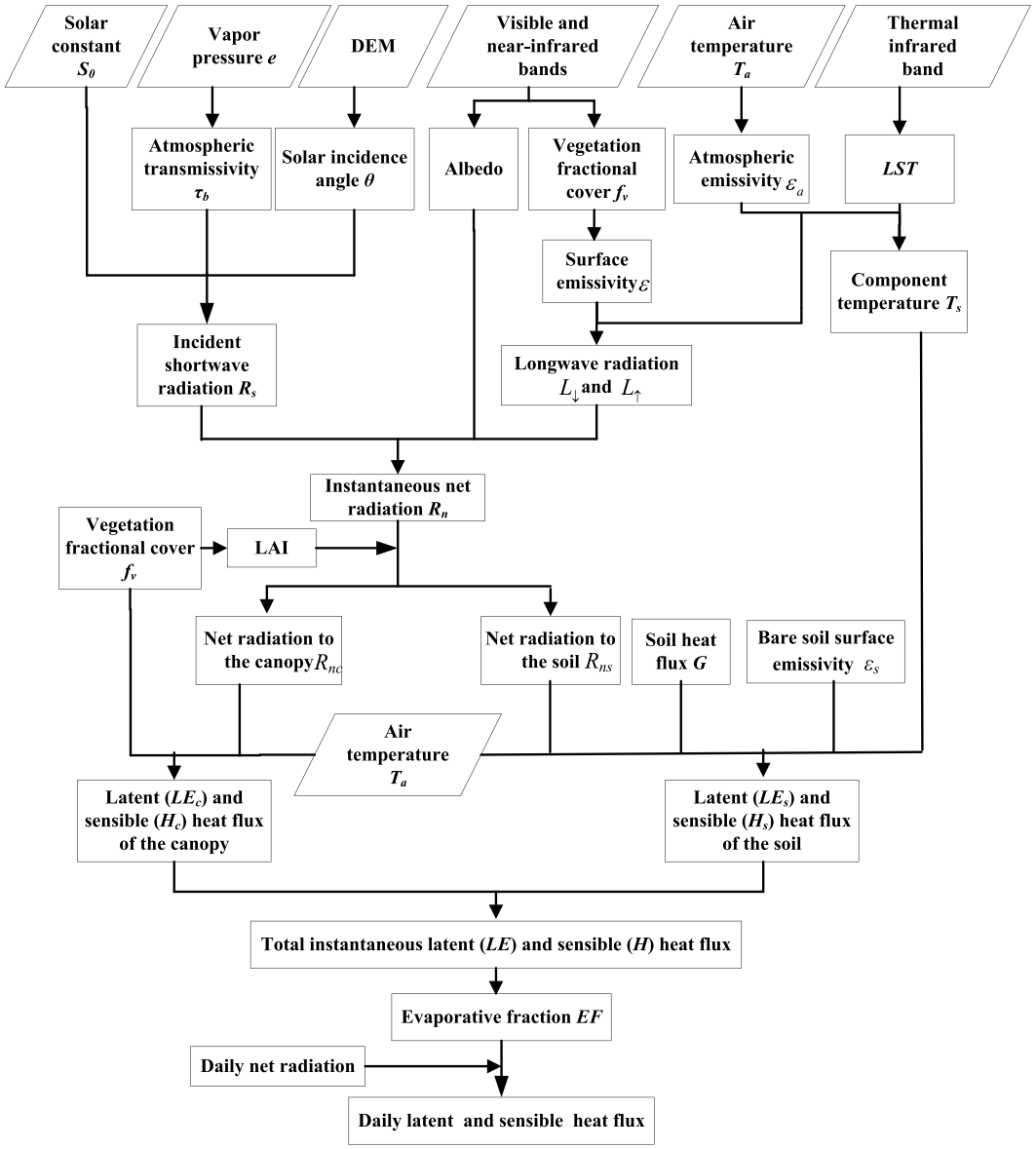

Figure 3. Flow chart of TD-TSEB, where trapezoids represent input variables and rectangles represent intermediate variables.

The variation ranges were set as ±20% for all input variables, incrementing by 5%. The sensitivity coefficient was also conducted using the data from the Daman (DM) site on DOY (day of year) 176, which were representative of a wider range of surface soil moisture and vegetation fractional cover.

2.4. Comparison With Other LE Models

2.4.1. The Original Two-Source Energy Balance (N95-TSEB) Model

The original two-source energy balance (N95-TSEB) model, developed by *Norman et al.* [1995], estimates the total LE as the sum of two components: transpiration and evaporation. The N95-TSEB model uses a layer network formulation to simulate the value of the energy exchange between the soil and canopy. In the N95-TSEB model, the PT equation is used to estimate of the canopy vegetation LE, but the PT parameter (a) is adjusted to 1.3. The PT iteration method is adopted to derive the component temperatures (i.e., soil and canopy temperatures) by providing an initial estimate of the canopy LE [*Norman et al.*, 1995; *Zhuang and Wu*, 2015]. The latent heat of soil evaporation is estimated using the residual of the surface energy balance (SEB) method. Excess resistance is introduced into the N95-TSEB model to offset the effects of using radiometric temperature in place of aerodynamic temperature [*French et al.*, 2015; *Sun and Mahrt*, 1995].

2.4.2. Satellite-Based Energy Balance for Mapping Evapotranspiration With Internalized Calibration (METRIC)

METRIC estimates LE using the residual of the SEB method from an OSEB model and calculates *H* from contextual image data [*Allen et al.*, 2007]. In this method, the apparent difference (*dT*) between LST and near-surface air temperature is resolved by assuming that the *dT* scales linearly with LST. The two coefficients of the linear equation between *dT* and LST are calculated contextually based on vegetation cover endpoints (hot and cold pixels) contained in the imagery, which is conducted through the examination of LST versus NDVI scatterplots [*Choi et al.*, 2009; *Liaqat and Choi*, 2015]. A major problem of METRIC is its method for selecting the extreme temperature values [*Long and Singh*, 2013]. Here reference LST values of the hot and cold reference pixels were selected based on cluster means, and cluster selection was based on LST statistics over the site and adjacent fields with cold and hot extremes chosen at 0.1% and 99.9% quantiles. *H* was then calculated through an iterative process based on the Monin-Obukhov similarity theory to illustrate stability effects on the aerodynamic resistance (r_{ah}) computed with an extrapolated *u* value for the top of the surface layer, as has been described elsewhere [*Allen et al.*, 2007; *Choi et al.*, 2009; *French et al.*, 2015].

3. Study Site and Data Processing

3.1. Study Site

This study was conducted at five agricultural cropping sites: Miyun (MY; 40.63°N, 117.32°E), Daxing (DX; 39.62°N, 116.43°E), Guantao (GT; 36.52°N, 115.13°E), Huailai (HL; 40.35°N, 115.79°E), and Daman (DM; 38.86°N, 100.37°E) (see Figure 4). Figure 4 also shows an example from the Landsat TM imagery of a 2.7 km by 4.7 km region (40.34°N–40.36°N and 115.78°E–115.84°E) that includes the HL site. The selected sites differ in crop types, elevation, and climatological characteristics (Table 2). The first four sites are included in the multiscale surface flux and meteorological elements observation data set for the Haihe River Basin of North China (*Haihe-Flux*) [*Liu et al.*, 2013; *Jia et al.*, 2012; *Y. Yang et al.*, 2015]. The DM site is included in the Multi-Scale Observation Experiment on Evapotranspiration over heterogeneous land surface which was part of the Heihe Water Allied Telemetry Experimental Research of Northwest China (HiWATER-MUSOEXE) [*Li et al.*, 2013; *Liu et al.*, 2011; *Song et al.*, 2016; *Xu et al.*, 2013].

MY is located in the northern mountainous area of the Haihe River basin at an elevation of 350 m above mean sea level. The source area of latent heat for MY is mainly contributed by orchard and maize, but it also mixes with bare land and buildings. DX is located in the central region of the Haihe River basin, and its dominant crops are winter wheat/maize and vegetables. GT is located in the North China Plain at an elevation of 30 m above mean sea level and GT's source area of winter wheat is mixed by seasonal maize and cotton. HL is in a semihumid and semidry area of the Haihe River basin that is entirely contributed by a pure signal of maize. DM has the highest elevation of the studied sites (1556 m). Irrigated maize dominates the agricultural ecosystem of this irrigation district of the Heihe River basin, but its source area of cropland is also mixed by bare land and roads.

3.2. Flux Tower Measurements

Half-hourly turbulent surface heat fluxes (LE, R_n, *H*, and *G*) and other climate data (such as T_a, *u*, atmospheric pressure, and relative humidity) were obtained from the four EC *Haihe-Flux* (http://westdc.westgis.ac.cn/haihe/) sites and one HiWATER-MUSOEXE (http://westdc.westgis.ac.cn/hiwater/) site under the fair-use policy. All of these sites are equipped with open path EC systems for monitoring water, energy, and carbon exchanges of the crops, soil, and atmosphere. The EC system includes a 3D sonic anemometer (CSAT3, Campbell Scientific Inc., USA) that measures three-dimensional velocity and temperature, as well as an open-path infrared CO_2/H_2O gas analyzer (Li-7500, Li-Cor, USA) that measures CO_2 and H_2O density [*Liu et al.*, 2013; *Xu et al.*, 2013]. The installation heights of the EC systems were 26.66, 3.0, 15.6, 5.0, and 4.5 m at the MY, DX, GT, HL, and DM sites, respectively. Postprocessing of the raw data recorded by the EC systems included sonic temperature, coordinate corrections, and gap filling using the EdiRe software (University of Edinburgh, http://www.geos.ed.ac.uk/abs/research/micromet/EdiRe). More details about the measurements and data postprocessing are given by *Liu et al.* [2011].

At the DM site, the isotopic composition of water vapor in surface air was determined based on water vapor isotopes measured with cavity ring-down spectroscopy water vapor isotope (ModelL1102-I, Picarro Inc)

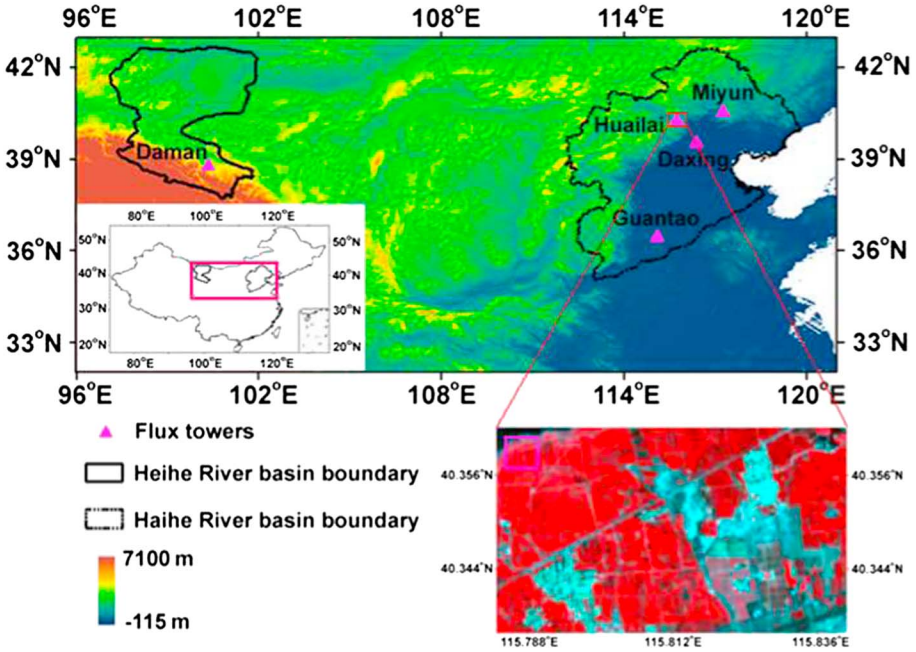

Figure 4. Locations of the five crop flux towers across northern China and an example of a small region that includes the Huailai site with a false-color composite from Landsat TM imagery acquired on 10 August (DOY 222) 2014.

[*Huang and Wen*, 2014; *Wen et al.*, 2016]. Two intakes of the eight-way solenoid valve at heights of 0.5 and 1.5 m above the corn canopy, respectively, were used to measure an ambient air sample [*Huang and Wen*, 2014; *Song et al.*, 2016]. The LE of soil evaporation (δ_E) was then determined using the *Craig and Gordon*'s [1965] model, and the LE of vegetation transpiration (δ_T) was estimated based on the δD and $\delta^{18}O$ of water in xylem when the isotopic state was satisfied at midday in field conditions [*Wen et al.*, 2016]. As water vapor contains unique isotopic signals of soil evaporation and canopy transpiration, the measured isotopic composition of the water could reasonably partition the measured LE (δ_{ET}) into δ_E and δ_T [*Hu et al.*, 2014; *Wen et al.*, 2012]. Although δ_{ET}, δ_E, and δ_T are affected by the isotopic state, irrigation, and strong advection, the measured data collected during the satellite overpass are reliable for this study.

3.3. Satellite and Ancillary Data

There were 69 cloud-free high-resolution Landsat TM/ETM+ thermal and visible shortwave images (resampled to 30 m resolution with a linear interpolation method) used herein. These data were downloaded from the Global Visualization Viewer webpage of the USGS (United States Geological Survey) (http://glovis.usgs.gov/). The at-satellite reflectance was converted to at-surface reflectance using atmospheric radiation transfer simulation models (e.g., MODerate resolution atmospheric TRANsmission) combined with atmospheric correction functions [*Tasumi et al.*, 2008].

T_a is a key input of the TD-TSEB model. To maintain high accuracy in this study, T_a was obtained directly from ground observations at the EC flux tower sites and was set to a fixed value to estimate R_n and LE across each region. This is performed to represent relatively homogenous atmospheric conditions within a small region. For terrain variables, such as elevation, slope, and aspect, which are used to estimate incident surface solar radiation (R_s), digital elevation models with 30 m spatial resolution were acquired from the NASA Land Processes Distributed Active Archive Center website (http://www.dgem.aster.ersdac.or.jp/index.jsp).

3.4. Variable Derivation

Surface broadband albedo with 30 m spatial resolution from five channels recorded in the Landsat TM/ETM+ data was retrieved using Liang's algorithm [*Liang*, 2000]. Coincident satellite data, such as the NDVI, surface

Table 2. Locations of the Five EC Flux Towers Used in This Study[a]

Site Name (Abbreviation)	Lat, Lon	Crop Types	Elevation (m)	Mean Annual Air Temperature (°C)	Average Annual Precipitation (mm/year)	Number of Landsat Images With No Cloud	Time Period
Miyun (MY)	40.63°N, 117.32°E	orchard and maize	350	10.9	615	29	1 Jan 2008 to 31 Dec 2010
Daxing (DX)	39.62°N, 116.43°E	winter wheat/maize and vegetables	20	11.6	556	6	1 Jan 2008 to 31 Dec 2010
Guantao (GT)	36.52°N, 115.13°E	winter wheat/maize and cotton	30	14.0	549	14	1 Jan 2008 to 31 Dec 2010
Huailai (HL)	40.35°N, 115.79°E	maize	480	10.1	370	15	1 Jan 2013 to 31 Dec 2014
Daman (DM)	38.86°N, 100.37°E	irrigated maize	1556	7.3	130	5	1 Jun 2012 to 30 Sep 2012

[a]All sites are located in "semihumid and semiarid" climate zone, except for DM site, which is "arid and semiarid."

emissivity (ε), and LST, were used for this study. Based on equations (3) and (4), ε was calculated using an empirical algorithm proposed by *Tasumi* [2003]. The accuracy of LAI retrieval depends on soil and crop types, and equation (3) may require local calibration. However, the impact of error in the LAI on R_n estimation was small in this study. LST was derived from the thermal infrared band (TIR, band 6) of Landsat TM/ETM+ images using a monowindow algorithm [*Qin et al.*, 2001] (Text S2). The satellite-derived LST is related to the soil and vegetation component temperatures [*Kustas and Anderson*, 2009]: T_s is calculated using the LST separation method proposed by *Lhomme et al.* [1994]:

$$\mathrm{LST} \approx (1 - f_v)T_s + f_v T_c; \text{and} \tag{23}$$

$$T_s - T_c = C_a(\mathrm{LST} - T_a)^m, \tag{24}$$

where T_c is the vegetation canopy temperature (°C) and C_a and m are the unitless empirical coefficients given by *Lhomme et al.* [1994]: $C_a = 0.1$ and $m = 2$.

Instantaneous R_n was calculated using instantaneous surface incident shortwave radiation (R_s), albedo, the instantaneous downward ($L_\downarrow$), and upward ($L_\uparrow$) longwave radiation fluxes. Daily R_n is estimated using the Slob function and extreme pixel LST [*Allen et al.*, 2007; *De Bruin and Stricker*, 2000] (Text S3).

4. Results

4.1. Validation of the TD-TSEB Model

4.1.1. Validation of the Estimated Instantaneous Surface Fluxes

To evaluate the accuracy of the TD-TSEB model, we compared the estimated instantaneous energy balance components (R_n, G, LE, and H) using the Landsat TM/ETM+ images with the tower-based flux measurements. We averaged the estimated surface fluxes over the upwind source area/footprint (ranging from 30 m to 120 m depending on u) for each flux tower. Figure 5 shows the good agreement between the four estimated instantaneous components of the energy balance equation versus the tower-based flux measurements. The squared correlation coefficients (R^2) for the comparison between the ground-measured and estimated instantaneous R_n values across all five sites were as high as 0.97 ($p < 0.01$), whereas the bias and root-mean-square-error (RMSE) values were 1.4 and 24.9 W/m^2, respectively. For the individual sites, underestimations of 2.6 and 11.7 W/m^2 were observed for instantaneous R_n at the MY and DX sites, respectively, whereas a slight overestimation was found for all other sites (Table 3). The biases in R_n are caused by propagated errors from EC ground-measured data, R_s, albedo, LST, ε, and differences in spatial resolution. The estimated instantaneous G derived from a fraction (0.31) of R_{ns} compared with tower-based measurements yielded an R^2 of 0.60 ($p < 0.01$), an RMSE of 26.7 W/m^2, and a bias of 1.4 W/m^2 across all five flux tower sites. Table 3 provides the statistics of overestimations (GT, HL, and DM) and underestimations (MY and DX) of instantaneous G, with an average RMSE of 25.7 W/m^2 and a bias of 1.9 W/m^2. Moreover, the accuracy of instantaneous G estimates

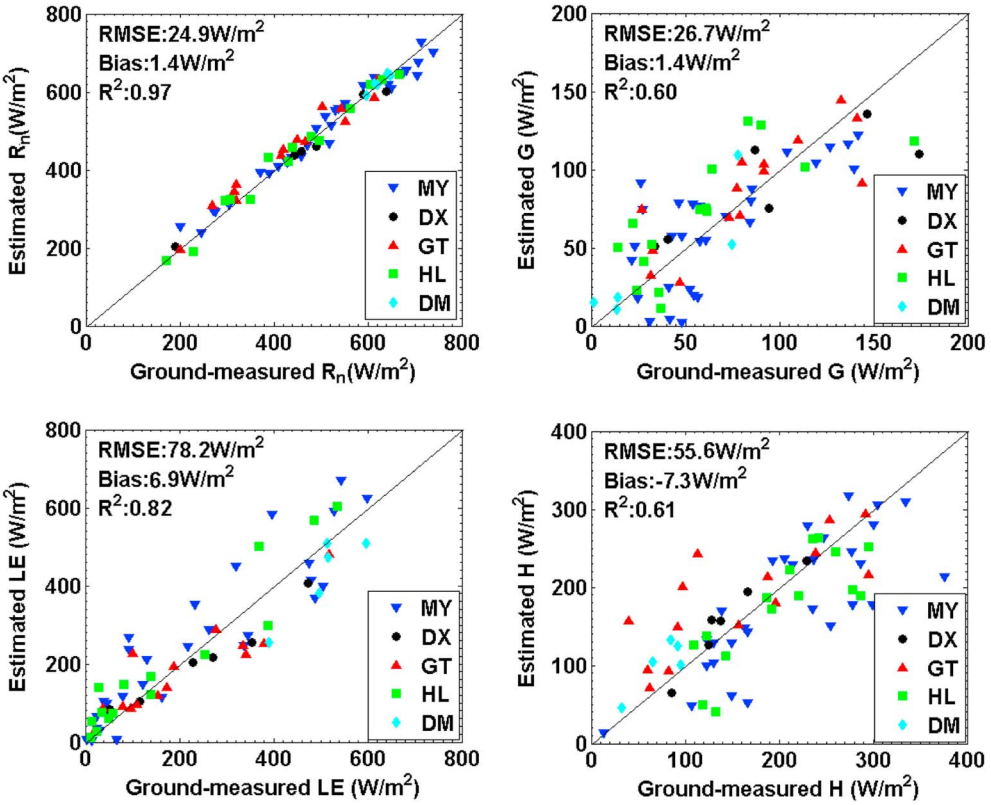

Figure 5. Comparison of the estimated instantaneous R_n, G, LE, and H values from the TD-TSEB model using Landsat TM/ETM+ images with corresponding ground measurements from all five sites.

was lower for the DX and HL sites than for other three crop sites. This may be principally caused by the simple fixed fraction used for G estimations that was not calibrated with ground observations because of a lack of data.

The instantaneous LE estimated with the TD-TSEB model agrees well with the tower-based measurements (Figure 5). In general, the R^2 of the LE values across all five sites was 0.82 (99% confidence), the RMSE was 78.2 W/m^2, and the bias was 6.9 W/m^2. By site, the TD-TSEB model explained 83%, 95%, 80%, 90%, and 81% of the observed variations in instantaneous LE for the MY, DX, GT, HL, and DM sites, respectively (Table 4). The highest RMSE of the estimated LE, with a value of 89.8 W/m^2, occurred at the DM site because of the presence of atmospheric advection and high soil moisture in this irrigated oasis region. In contrast, for the DX site, the estimated instantaneous LE yielded the lowest RMSE, 57.3 W/m^2, and a negative bias of -36.4 W/m^2, which may be principally attributed to the relatively few samples (only six Landsat TM/ETM+ scenes) and the good performance of the TD-TSEB model for winter wheat/maize and vegetables fields. In addition, the TD-TSEB model yields instantaneous LE for other crops reasonably well; the RMSE for the orchards and maize fields of MY was 85.6 W/m^2; for the winter wheat/maize and cotton fields of GT, it was 64.7 W/m^2; and for the maize fields of HL, it was 63.4 W/m^2 (Table 4). These favorable results may indicate the applicability of the TD-TSEB model to fields with higher vegetation fractions associated with coupling the signal of the visible and near-infrared and thermal infrared (TIR) bands of the Landsat TM/ETM+ images.

The calculated instantaneous H based on R_n and the TD-TSEB model has an R^2 of 0.61 ($p < 0.01$), an RMSE of 55.6 W/m^2, and a bias of -7.3 W/m^2 across all five sites (Figure 5). As shown in Table 4, the largest RMSE (61.6 W/m^2) and the second largest RMSE (61.2 W/m^2) occurred at the GT and MY sites, respectively, which may be explained by uncertainty of the EC measurements caused by the heterogeneity of the underlying surfaces. For the other three sites, the estimated instantaneous H values showed good agreement with the tower-based measurements, with RMSEs of 20.8, 49.5, and 32.1 W/m^2 for the DX, HL, and DM sites,

Table 3. Summary Statistics Comparing Between the Ground-Measured and Estimated R_n and G in This Study: Bias, Root-Mean-Square Error (RMSE), and the Square of the Correlation Coefficients (R^2)[a]

Energy Component	Site Name	Mean Observed Values (W/m^2)	Bias (W/m^2)	RMSE (W/m^2)	R^2
Instantaneous Components					
R_n	MY	505.3	−2.6	27.2	0.97
	DX	469.1	−11.7	20.9	0.98
	GT	429.4	16.3	29.1	0.96
	HL	444.3	0.8	21.2	0.98
	DM	624.1	0.3	5.6	0.92
	Overall	482.1	1.4	24.9	0.97
G	MY	65.9	−3.8	27.1	0.52
	DX	96.1	−6.1	30.9	0.69
	GT	82.7	3.5	22.3	0.67
	HL	59.7	11.5	29.8	0.57
	DM	36.4	4.6	18.4	0.77
	Overall	68.4	1.4	26.7	0.60
Daily Components					
R_n	MY	138.1	0.3	13.4	0.95
	DX	157.9	−3.3	15.1	0.89
	GT	108.2	6.8	19.1	0.86
	HL	119.2	4.6	20.8	0.81
	DM	166.3	−1.3	8.6	0.98
	Overall	129.4	2.1	16.4	0.90
G	MY	21.9	0.9	8.7	0.49
	DX	18.5	6.7	10.8	0.50
	GT	17.5	4.6	7.6	0.60
	HL	20.5	4.4	10.5	0.58
	DM	12.4	2.5	6.6	0.73
	Overall	19.7	3.0	8.9	0.51

[a]All correlation coefficients are significant with 99% confidence.

respectively. However, H was not directly estimated using the TD-TSEB model but calculated as the residual of the energy balance equation. Therefore, erroneous results in the estimation of H are caused not only by the biases in many parameters (e.g., R_s, albedo, LST, and T_a,) between the land surface and atmosphere but also by the errors in EC flux measurements.

4.1.2. Validation of the Estimated Daily Surface Fluxes

Figure 6 and Tables 3 and 4 present statistical comparisons of the estimated daily surface fluxes (R_n, G, LE, and H) with the corresponding flux-tower measurements that were scaled-up from the instantaneous values. This comparison shows that the estimated daily R_n has an R^2 of 0.90 ($p < 0.01$), an RMSE of 16.4 W/m^2, and a bias of 2.1 W/m^2 across all five sites. When compared with the estimated instantaneous R_n values, there was slightly worse agreement between the estimated daily R_n versus the ground measurements (Table 3). Given that only a single instantaneous R_n was used to scaled up for each daily values, the relatively small errors identified in this study show that it is more feasible to apply the Slob function and the extreme pixel LST method to estimate daily R_n. For different crop types, the bias of the estimated daily G varies from 0.9 to 6.7 W/m^2, the R^2 (99% confidence) varies from 0.49 to 0.73, and the RMSE varies from 6.6 to 10.8 W/m^2 (Table 3). Similar to the estimated instantaneous G, a local calibration coefficient for the daily G algorithm may contribute to improving the performance of the simple algorithm used to calculate daily G in this study.

The TD-TSEB model was able to account for 86% of the observed daily LE variation. The estimated daily LE had a bias of 1.4 W/m^2 and an RMSE of 21.4 W/m^2 across all sites (Figure 6 and Table 4). However, the model underestimated daily LE at the DM site with an RMSE higher than 39 W/m^2, which was likely a result of the underestimated instantaneous LE. At the other four sites, the TD-TSEB model gave accurate predictions with RMSE values lower than 23 W/m^2. Despite the good agreement between the estimated daily LE and ground measurements, the TD-TSEB model shows a relatively low performance for daily H estimates: the overall R^2 (99% confidence) of the estimated daily H across all sites was 0.65, and the RMSE was 18.2 W/m^2 (Figure 6 and Table 4). The accumulated errors from the daily R_n, G, and LE may have resulted in these inaccurate daily H

Table 4. Summary Statistics Comparing the Ground-Measured and Estimated LE and *H* Using TD-TSEB, N95-TSEB, and METRIC: Bias, Root-Mean-Square Error (RMSE), and the Square of the Correlation Coefficients (R^2)[a]

			Td-TSEB			N95-TSEB			METRIC		
Energy Component	Site Name	Mean Observed Values (W/m^2)	Bias (W/m^2)	RMSE (W/m^2)	R^2	Bias (W/m^2)	RMSE (W/m^2)	R^2	Bias (W/m^2)	RMSE (W/m^2)	R^2
Instantaneous Components											
LE	MY	231.5	27.2	85.6	0.83	26.3	92.8	0.80	26.4	90.4	0.75
	DX	249.5	−36.4	57.3	0.95	−6.6	39.3	0.93	19.2	41.3	0.90
	GT	200.8	−17.2	64.7	0.80	−23.1	65.7	0.78	−18.3	65.6	0.81
	HL	174.3	31.3	63.4	0.90	20.9	69.8	0.91	29.7	63.5	0.87
	DM	503.4	−63.6	89.8	0.81	−58.8	82.3	0.78	−60.5	89.6	0.84
	Overall	234.1	6.9	78.2	0.82	6.1	79.7	0.80	11.1	81.7	0.81
H	MY	210.6	−27.5	61.2	0.61	−29.5	79.1	0.55	−21.9	62.4	0.52
	DX	145.4	11.2	20.8	0.91	−25.8	37.4	0.91	−18.3	39.6	0.91
	GT	154.8	31.6	61.6	0.61	21.4	60.8	0.60	15.4	61.2	0.59
	HL	202.2	−23.8	49.5	0.63	12.2	64.7	0.63	−6.7	46.5	0.60
	DM	74.1	28.3	32.1	0.73	25.6	32.3	0.66	33.2	39.7	0.74
	Overall	181.9	−7.3	55.6	0.61	−5.8	58.2	0.57	−6.7	57.8	0.58
Daily Components											
LE	MY	68.1	8.5	17.6	0.94	10.8	22.5	0.90	8.3	21.6	0.85
	DX	81.9	−16.6	22.5	0.90	−10.3	18.3	0.87	−11.8	19.2	0.84
	GT	54.0	−1.1	18.4	0.82	−1.7	20.1	0.82	−1.3	20.1	0.82
	HL	56.6	6.8	18.9	0.90	−0.8	21.4	0.91	4.7	20.3	0.92
	DM	143.9	−27.4	39.9	0.62	−19.2	31.6	0.72	−20.5	32.7	0.72
	Overall	69.4	1.4	21.4	0.86	1.7	21.9	0.85	1.7	22.5	0.84
H	MY	59.8	−10.1	19.3	0.66	−9.6	21.6	0.66	−14.4	23.9	0.63
	DX	36.3	−2.6	10.3	0.62	−2.9	11.7	0.58	−3.8	12.6	0.65
	GT	42.8	−0.4	15.1	0.72	3.8	20.4	0.61	3.5	21.7	0.57
	HL	51.5	−3.9	21.7	0.52	3.4	19.1	0.57	−2.9	20.2	0.51
	DM	12.5	12.8	15.8	0.91	7.9	13.2	0.85	9.1	13.3	0.81
	Overall	49.1	−4.5	18.2	0.65	−2.2	19.8	0.61	−5.6	20.3	0.60

[a]All correlation coefficients are significant with 99% confidence.

estimates. However, large differences between the estimated and observed daily *H* occurred in different crop types. For example, the TD-TSEB model performed very well for estimating daily *H* in most mixed-crop ecosystem, but it substantially underestimated the daily *H* for the orchards and maize fields. The model's performance was similar in estimating instantaneous *H*.

4.1.3. Validation of the Partition of LE Estimates Into Soil and Canopy

The TD-TSEB model provides estimates of the total LE partitioned to the soil (LE_{soil}, i.e., $(1-f_v)\times LE_s$) and the canopy (LE_{canopy}, i.e., $f_v \times LE_c$). There have been very few studies to focus on validation of LE_{soil} and LE_{canopy} using reliable component measurements [*Song et al.*, 2016; *Xiong et al.*, 2015]. Because the components of daily EF for both soil evaporation and canopy transpiration were not distinguished, we could only validate the partitioning of instantaneous LE estimates into soil and canopy components in this study. The stable oxygen and hydrogen isotope method based on DOY 160, 176, 215, 224, and 240 was used to measure the instantaneous ratios of LE_{soil}/LE and LE_{canopy}/LE to separate LE_{soil} and LE_{canopy} at the DM site. Figure 7 shows that the estimated instantaneous LE_{soil} based on the TD-TSEB model had an R^2 of 0.44 ($p = 0.05$), an RMSE of 16.5 W/m^2, and a bias of −4.2 W/m^2. Similarly, for instantaneous LE_{canopy}, the TD-TSEB model yielded an R^2 of 0.77 ($p < 0.05$), an RMSE of 91.3 W/m^2, and a bias of −60.1 W/m^2. Figure 8 illustrates that the TD-TSEB model had good accuracy for the LE_{soil}/LE ratio, with an average bias of 11.1%, which is lower than the bias reported in previous studies [*Kang et al.*, 2005; *Song et al.*, 2016].

The LE_{soil}/LE ratio estimated with the TD-TSEB model has similar seasonal variation and is in agreement with the ground observations (Figure 8) for most days (excluding DOY 176). Because of the lack of sufficient auxiliary information, it is difficult to evaluate the possible causes of the relatively large discrepancies found for DOY 176. It may be related to relatively high LST (LST = 29.28°C) retrieved at Landsat TM overpass time on this day when compared with values retrieved on DOY 160 (LST = 23.35°C) and DOY 215(LST = 25.71°C). Although some previous studies have documented that isotope approaches are often associated with lower values for

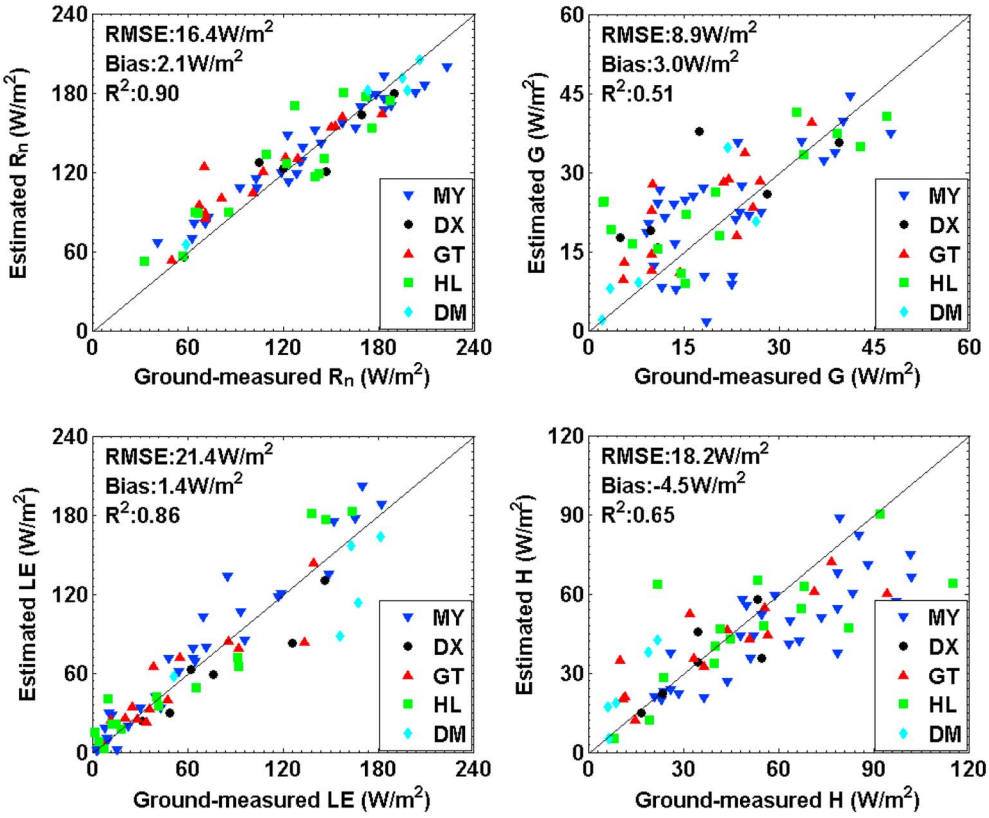

Figure 6. Comparison of the estimated daily R_n, G, LE, and H values from the TD-TSEB model using Landsat TM/ETM+ images with corresponding ground measurements from all five sites.

the LE_{soil}/LE ratio [*Schlesinger and Jasechko*, 2014], the strong validation results indicate that the TD-TSEB model can be used to accurately partition LE into the latent heats of vegetation transpiration and soil evaporation.

4.2. Sensitivity Analysis

The sensitivity of the TD-TSEB model to the R_s was determined to be the highest, and the R_s is positively correlated with LE (Figure 9 and Table 5). Because R_s is the main energy source for LE, LE increased relatively by up to ±25% when R_s changed by ±20%. The second largest changes of LE were caused by the variation of NDVI. In response to the changes in LE of ±20%, the NDVI varies accordingly by −22.3% to 16.7%. LST is negatively correlated with LE, but T_a is positively correlated with LE. Increases in LST and T_a by 1 K were associated

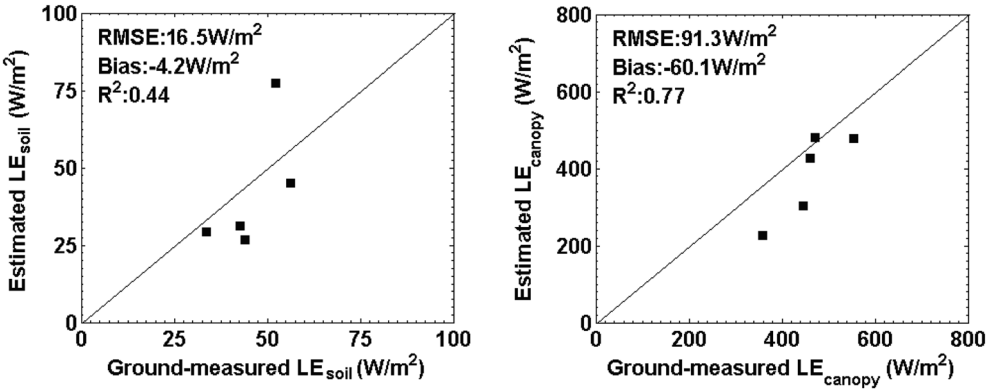

Figure 7. Comparison of the estimated instantaneous LE_{soil} and LE_{canopy} values from the TD-TSEB model using Landsat TM/ETM+ images with corresponding ground measurements from the DM site.

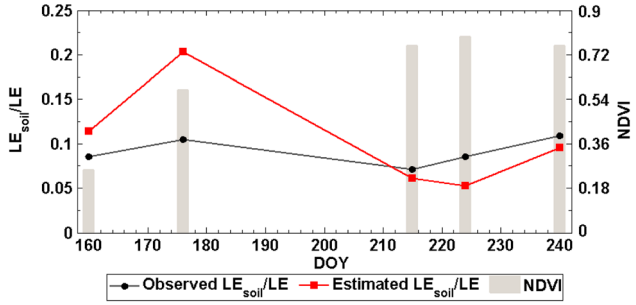

Figure 8. Comparison of TD-TSEB-based estimates and ground measurements of LE_{soil}/LE for the DM site.

with a 1.9% decrease and a 1.6% increase, respectively, in the estimated LE, whereas decreases in LST and T_a by 1 K resulted in a 1% increase and a 3.4% decrease in LE estimates, respectively. The surface albedo is used only in the calculation of R_n in the TD-TSEB model, and it has a negative effect on LE. Changes in LE were as large as ±4.4% for albedo changes of ±20%. Overall, LE estimation by the TD-TSEB model showed a distinct order of sensitivity as follows: $R_s >$ NDVI $> T_a >$ LST $>$ albedo.

4.3. Comparison With Other LE Models

Given that the pointed-based ground observations are a suitable method for perform model validation and comparison, the estimated LE and *H* at site scale based on the TD-TSEB model were compared with those obtained using N95-TSEB and METRIC. The statistics for comparing these two additional models (N95-TSEB and METRIC) with ground-measured instantaneous LE (*H*) are provided in Table 4. We noted that the RMSE of the estimated instantaneous LE (*H*) values from N95-TSEB varies from 39.3 (32.3) to 92.8 (79.1) W/m^2 and that R^2 ($p < 0.01$) varies from 0.78 (0.55) to 0.93 (0.91). Similarly, METRIC yields instantaneous LE (*H*) values with RMSEs that range from 41.3 (39.6) to 90.4 (62.4) W/m^2 and with R^2 values with 99% confidence that range from 0.75 (0.52) to 0.90(0.91). Overall, these two models provide reasonable accuracy. Importantly, graphical comparisons of instantaneous LE (*H*) estimated with the TD-TSEB model and the two additional models illustrate that there is good agreement between the TD-TSEB model and other two models (Figure 10), as well as similar statistical results when compared with the flux observations. The obvious differences among the models are that TD-TSEB tends to estimate slightly higher values of LE compared to METRIC for high vegetation cover conditions, whereas it estimates slightly lower values of LE compared to N95-TSEB for high vegetation cover conditions. The agreement among the different models and the flux observations indicates that TD-TSEB performs well with a comparable accuracy as the more complex TSEB models and simple OSEB models.

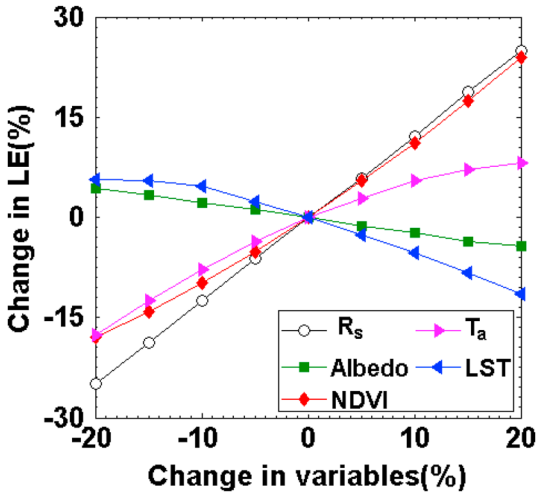

Figure 9. Sensitivity analysis of the TD-TSEB model to the R_s, albedo, NDVI, T_a, and LST specified between −20% and 20%, incrementing by 5%.

Table 5. Relative Sensitivity Coefficient S_v (%) of LE Estimates From TD-TSEB to Each Input Variable at the DM Site on DOY 176[a]

Variation (%)	R_s	Albedo	NDVI	T_a	LST
−20	−25	4.4	−17.9	−17.7	5.7
−15	−18.7	3.3	−14.1	−12.5	5.5
−10	−12.5	2.1	−9.8	−7.8	4.7
−5	−6.2	1.1	−5.2	−3.6	2.3
5	5.9	−1.3	5.5	2.8	−2.6
10	12.2	−2.3	11.2	5.5	−5.4
15	18.5	−3.6	17.4	7.1	−8.3
20	24.7	−4.7	23.9	7.5	−11.4

[a]Variations of variables are in percentage (%).

Both Table 4 and Figure 11 present the daily LE and *H* results from the comparisons of the two models, and we draw a similar conclusion that TD-TSEB has provided a comparable accuracy as other TIR-based LE models for quantifying daily LE and *H*. Therefore, it is appropriate to apply TD-TSEB to estimate surface fluxes under this set of environmental conditions.

4.4. A Case Study of Mapping Field LE With the TD-TSEB Model

Figure 12 shows an example of spatial patterns in instantaneous field LE, daily LE, LE_s, and LE_c, as well as the corresponding NDVI, from the TD-TSEB model for 3 days over a small region that includes the HL site described in section 3.1. On DOY 158, the estimated LE_c and LE_s had the smallest spatial variations across the images which correspond to the narrowest spatial variations in the NDVI. These spatial variations reached their largest on DOY 222 when the NDVI also reached its maximum value. Smaller spatial variations occurred in the maps of LE_c and LE_s on DOY 240 with a decreasing NDVI for most pixels. The spatial

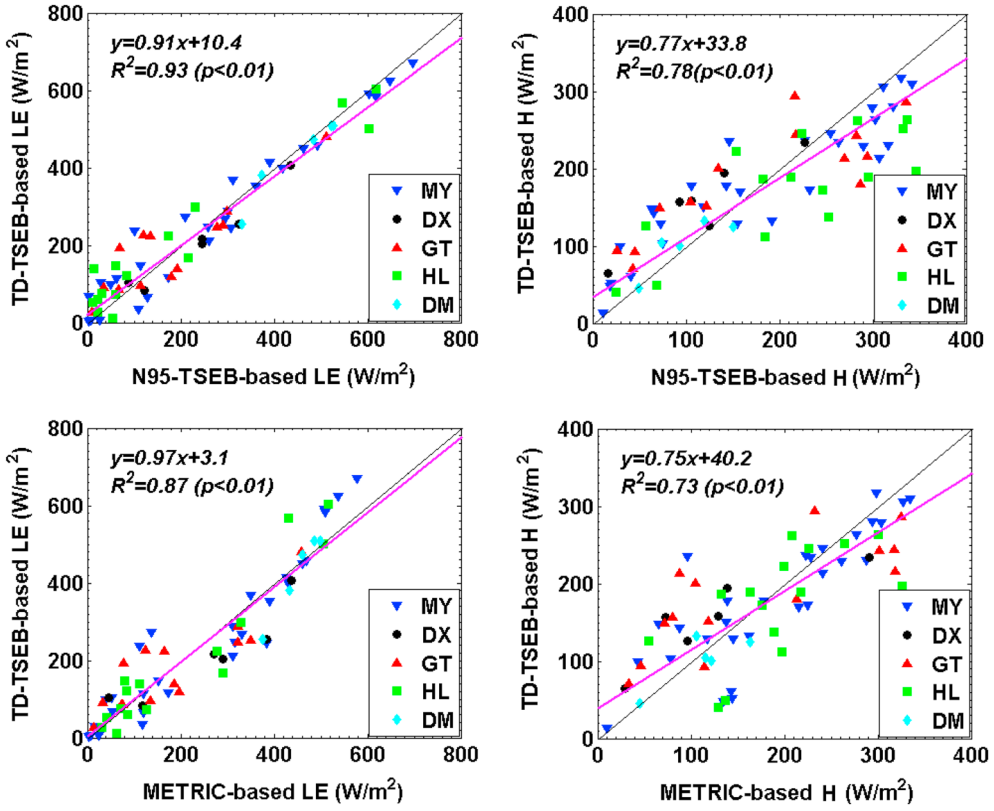

Figure 10. Linear regressions between the instantaneous surface energy fluxes (LE and *H*) estimated with the TD-TSEB model versus the results of two other models (the N95-TSEB model and METRIC) for all five sites. The black line is the 1:1 line, and the line-of-best-fit is the pink line which is given by the equation on each sub-plot.

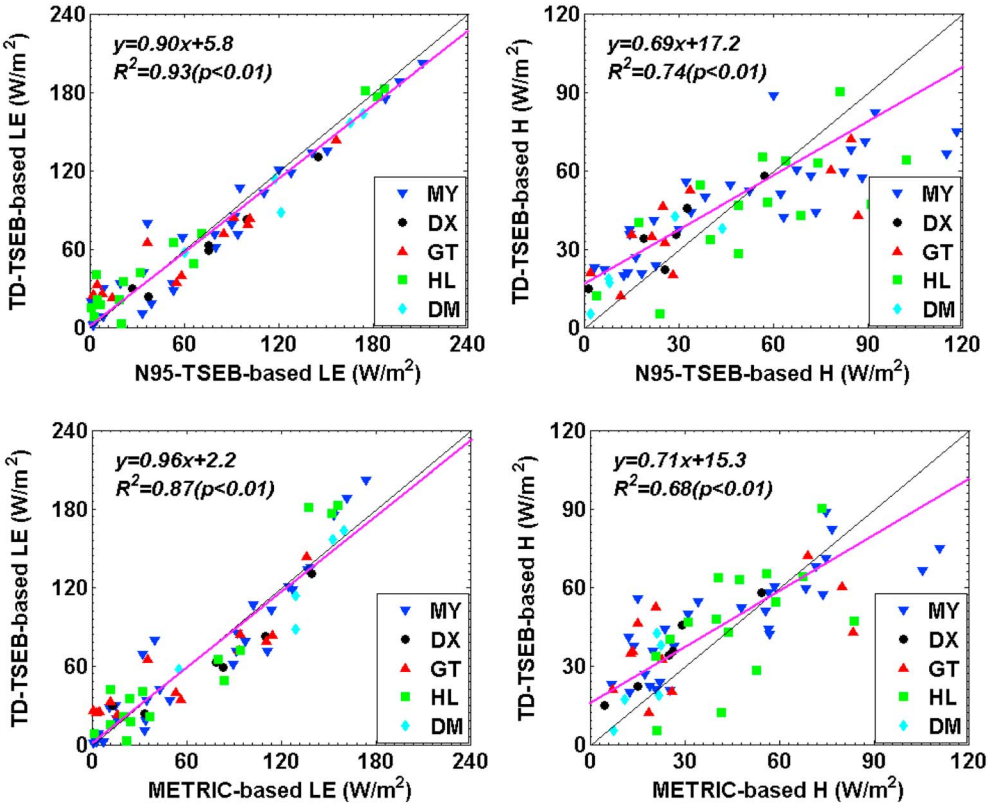

Figure 11. Linear regressions between the daily surface energy fluxes (LE and *H*) estimated with the TD-TSEB model versus the results of the other two models (the N95-TSEB model and METRIC) for all five sites. The black line is the 1:1 line, and the line-of-best-fit is the pink line which is given by the equation on each sub-plot.

variations in instantaneous and daily LE are similar to the results for the corresponding LE_c and LE_s flux components (Figure 12).

The maps of LE_c are strongly positively correlated with the NDVI ($R^2 = 0.94$) whereas LE_s is strongly negatively correlated with the NDVI ($R^2 = 0.81$). This phenomenon may be explained by the fact that LE_c is higher and LE_s lower, where there is a higher vegetation fractional cover. Based on thermal remote sensing, the TD-TSEB model detected few wet regions (e.g., pixel A) in which both the NDVI and LST are low in the top left part of the domain in which LE_s was high (Figure 13). These fields were covered with wet soil and a small amount of crop on DOY 222, and the mixture of soil and crop in these regions may not be accurately reflected in the NDVI, but would be captured by the LST in real time because of the effects of soil moisture, *u*, and R_{ns}. Therefore, LE algorithms that only use vegetation indices sensitive to vegetation fractional cover may not identify small differences in field LE.

5. Discussion

5.1. Sensitivity Analysis of the TD-TSEB Model

In the TD-TSEB model developed here, the results were more highly dependent on the NDVI than was found in the previous studies [*Granier and Breda*, 1996; *Norman et al.*, 1995]. This difference is because the TD-TSEB model includes the PT algorithm for estimating crop canopy transpiration, which is mainly determined by the variation of the NDVI. *Granier and Breda* [1996] reported that canopy resistance would be a crucial factor for crops and that seasonal variation of the LAI or the NDVI has great impact on crop canopy conductance and LE. This indicates that unlike other hydrologic and meteorological variables, NDVI plays a major role in a dormant season in the TD-TSEB model. Employment of NDVI with no model-related errors will reduce uncertainty of the TD-TSEB model [*Zhang et al.*, 2009].

The dependency of R_s in the TD-TSEB model is the highest than the NDVI, LST, T_a, and albedo because it drives the processes of evapotranspiration [*Hwang and Choi*, 2013; *Zhang et al.*, 2014]. The TD-TSEB model shows

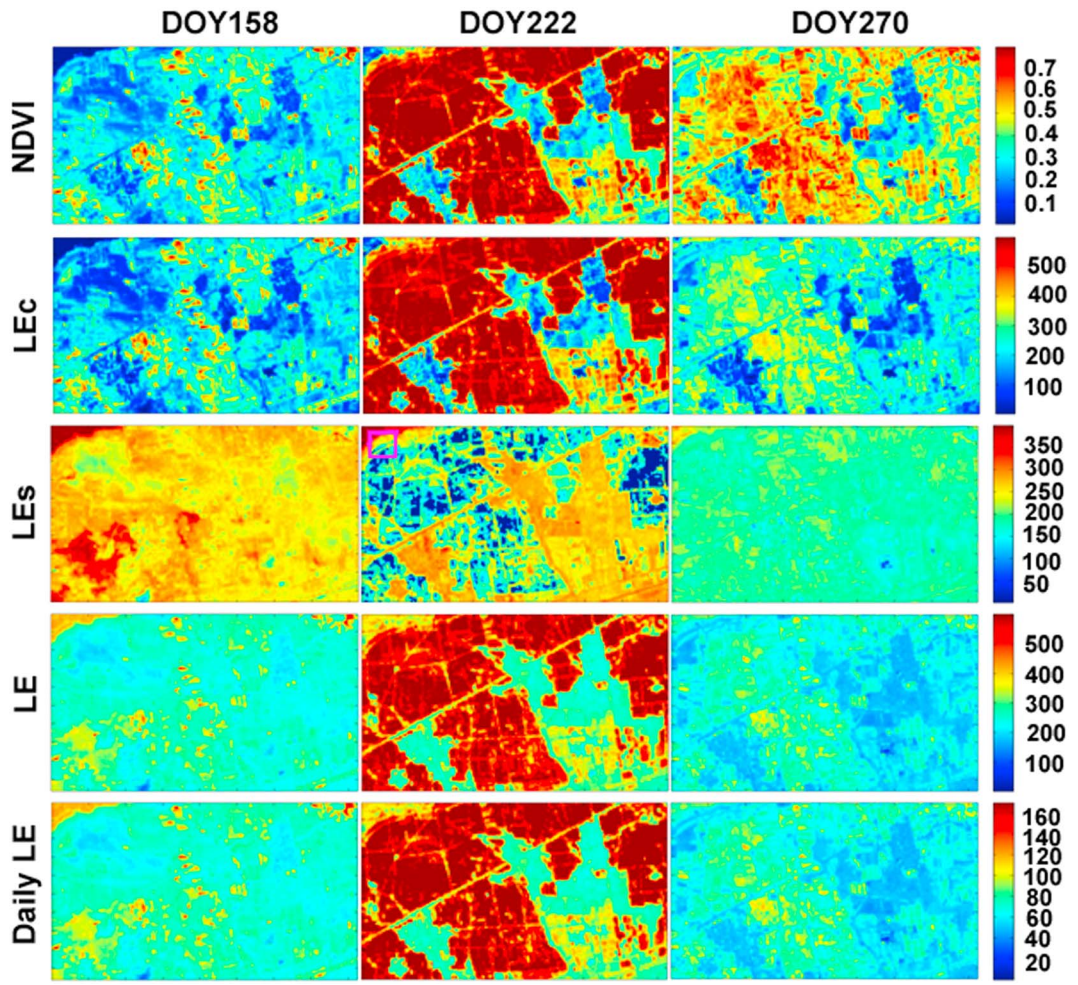

Figure 12. Example maps of the NDVI, LE_c (W/m^2), LE_s (W/m^2), instantaneous LE (W/m^2), and daily LE (W/m^2) produced with the TD-TSEB model for a small region that includes the HL site for 3 days in 2014. The pink area demarcated in the top left of the LE_s panel for DOY 222 is expanded in Figure 13.

less sensitivity to LST than other OSEB and TSEB models. *Yang and Shang* [2013] pointed out that increases in LST and T_a by 2 K would lead to a 23.2% decrease and a 15.3% increase, respectively, in estimated LE based on the hybrid dual-source scheme and trapezoid framework-based evapotranspiration model (HTEM). The variations in albedo would result in slight changes in LE, which indicates that the sensitivity of the TD-TSEB model to the albedo is lower than its sensitivity to other input variables.

5.2. Performance of the TD-TSEB Model

Model validation at five EC flux tower sites at crops across China has indicated that the TD-TSEB model for estimating field surface fluxes was reliable and robust across different crop types. Tables 3 and 4 show that the TD-TSEB model did not yield significant predictive errors for LE and *H* across most validation sites (excluding the DM site). One important reason for its predictively is that the TM/ETM+-based NDVI coupled with the TD-TSEB model captures the seasonal cycle of the crops to produce considerably accurate LE values. Many studies have indicated that most crops (e.g., winter wheat and maize) present strong seasonal changes in the LAI, leaf chlorophyll content, and red reflectance, and the NDVI derived from red and visible reflectance responds strongly to leaf chlorophyll, plant water potential, and CO_2 concentration [*Norman et al.*, 1995; *Tucker*, 1979; *Yan et al.*, 2012; *Yebra et al.*, 2013; *Zhang et al.*, 2009]. The variation in leaf chlorophyll concentration is often linked to changes in the stomatal conductance of crops [*Matsumoto et al.*, 2005] and accounts for the good performance of the NDVI for estimating LE_{canopy}. Another key reason for the success of this method is that T_s decomposed from TIR-derived LST provides valuable diagnostic information about

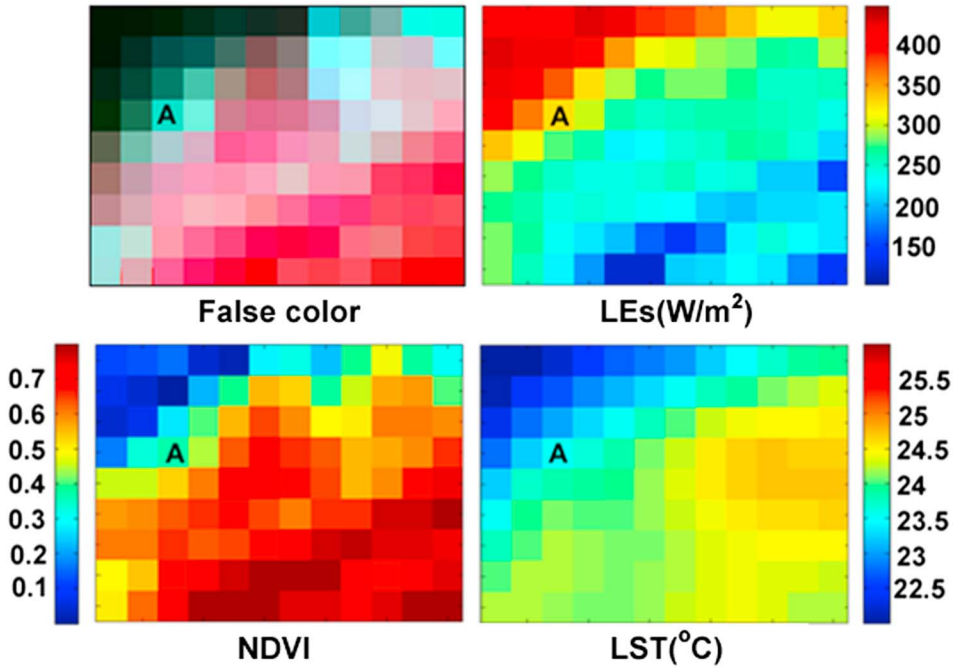

Figure 13. Expanded view of region demarcated by the pink square in Figure 12 (see specifically DOY 222 and the LE_s image) to highlight mixed regions (e.g., pixel A) with wet soil and a small amount of crops with a correspondingly low NDVI and LST.

subsurface moisture status to yield reliable LE_{soil} values. Recent studies have demonstrated that LST may be used as a surrogate for in situ surface moisture observations because T_s effectively integrates the effects of subsurface moisture by detecting the increase in T_s associated with the depletion of available surface moisture [*Anderson et al.*, 2008; *Gillies and Carlson*, 1995; *Zhan and Kustas*, 2001]. *Zhan and Kustas* [2001] found that estimated surface fluxes based on LST provide better agreement with ground-measured fluxes than those based directly on soil moisture directly. Although T_s derived through the empirical LST separation method [*Lhomme et al.*, 1994] may not be consistent with T_s values estimated using the Priestley-Taylor iteration approach [*Norman et al.*, 1995], it has nonetheless provided effective TIR information about soil evaporation and has yielded satisfactory estimates of *H* and LE over the multiple crop types studied herein.

Substantial underestimation of LE (a bias of -63.6 W/m^2) was found for the DM irrigated crop site. This finding illustrates that irrigation practice and strong advection would be more critical than maize canopy structure in determining TSEB model performance [*Zhang et al.*, 2012; *Song et al.*, 2016]. When considering the contributions of irrigation water and the atmospheric advection to LE, the performance of the TD-TSEB model may be significantly better in an advective humid environment. In contrast, the TD-TSEB model tends to overestimate LE slightly (bias of more than 25 W/m^2) at two sites: MY and HL. For example, the estimated instantaneous LE was higher than the ground-measured LE at the MY site with a bias value of 27.2 W/m^2 and an RMSE value of 85.6 W/m^2, respectively (Table 4). The PT coefficient (*a*) probably plays an important role in quantifying LE at these sites. For the TD-TSEB model, we used the PT model with coefficient *a* of 1.26 to estimated the LE_c for both stressed and unstressed vegetation and crops [*Priestley and Taylor*, 1972; *Fisher et al.*, 2008; *Yao et al.*, 2013]. However, the PT coefficient (*a*) built into the TD-TSEB model is not constant but varies with vegetation status, vegetation type, and vapor pressure deficit [*Priestley and Taylor*, 1972; *Long and Singh*, 2012]. Consequently, the TD-TSEB model may tend to overestimate LE under certain agricultural and natural settings.

The TD-TSEB model was found to be generally robust in the estimation of component flux; the estimated LE_{soil}/LE ratio varies from 0.06 to 0.22 over DOY 160–240. The large variability in LE_{soil}/LE is evident in most annual crops with the large seasonal variations in crop canopy cover fraction (i.e., from zero to full cover).

Previous studies have shown that in LE partitioning in cotton fields, average LE_{soil} was found to account for 20–30% of the LE [*Agam et al.*, 2012; *Lascano*, 2000]. The LE_{soil}/LE values for corn, wheat, and soybean fields were slightly higher and highly variable, with averages between 30% and 40% [*Denmead et al.*, 1996; *Kool et al.*, 2014; *Singer et al.*, 2010; *Zeggaf et al.*, 2008]. The TD-TSEB model yields results that are close to the ranges reported by previous studies.

A general difference between the TD-TSEB model and the other two models we assessed (N95-TSEB and METRIC) is that the TD-TSEB model combines the equilibrium evaporation and the variation in T_s based on a simplified framework of total aerodynamic resistance to estimate the LE_s. Although the TD-TSEB model uses T_s and T_a to simplify the Ohm's law-type equation, this method reduces the accumulated errors of input variables and yields comparable accuracy as the other two models. In fact, because different crop types have different aerodynamic resistances and the universal stability functions used to calculate aerodynamic resistance may result in large errors [*Sun et al.*, 1999; *Wang and Dickinson*, 2012].

The TD-TSEB algorithm uses Landsat TM/ETM+ data to provide spatially continuous field LE information, which significantly strengthens the model performance across regional scales. However, inaccuracy in the EC ground measurements, model input data errors, spatial scale mismatches between tower-specific and TM/ETM+ data, and the structure of the TD-TSEB model all affect the accuracy of the model. The typical error of the EC-measured LE is approximately 5–20% [*Foken*, 2008; *Mahrt*, 2010], and the temporal upscaling from half hours to days also results in a 5–10% bias in daily LE values [*Hui et al.*, 2004; *Jia et al.*, 2012; Van Niel et al., 2012]. Moreover, EC measurements do not conserve energy, and the averaged energy closure ratio across the five EC sites is 0.85, which may be partially attributed to the fact that the EC method cannot capture large eddies in the lower boundary layer but only measures small eddies [*Dawson et al.*, 2007; *Foken*, 2008; *Wilson et al.*, 2002]. Although *Twine et al.* [2000] proposed two methods to correct the energy balance closure, namely, by calculating the LE as a residual of the energy balance (*RE* method), and by conserving the measured Bowen ratio (BR method), there is no consensus on how to resolve lack of energy balance closure with eddy covariance [*Finnigan et al.*, 2003]. We directly compared model estimations with ground observations without closure and this undermeasured LE led to 5–15% bias for instantaneous LE estimation [*Finnigan et al.*, 2003]. Additionally, the errors in the ground measurement of other meteorological variables (e.g., T_a), satellite-derived R_n, T_s, LAI, and f_v, all introduce errors into the estimation of LE and *H*. For example, error in satellite-based LST from TM/ETM+ imagery has been reported to be 1°C [*Li et al.*, 2013; *Qin et al.*, 2001], which introduces error of more than 20% for instantaneous LE estimation.

The footprints of the EC measurements vary from several meters to tens of meters, because changes in measuring height (usually 2–30 m) result in changes in horizontal scaling of the measurement of turbulent fluxes [*Schmid*, 1997]. The tower measurement footprints are smaller than the resolution (about 30 m) of the biophysical parameters derived from TM/ETM+ imageries (e.g., NDVI, R_n, and resampled LST); consequently, these satellite-derived biophysical parameters may not adequately capture subpixel surface signals at the flux tower sites [*Kustas and Norman*, 1999; *Mu et al.*, 2011]. Therefore, inaccurate representation of the satellite-derived biophysical parameters of the tower footprint conditions may cause model error. Similarly, errors that propagate through the LST resampling also contribute to uncertainty in LE estimation. Additionally, the structure of the TD-TSEB model also influences the accuracy of LE estimation because it ignores the differences in crop stomatal conductance (characterized by f_v in this study) among different crop types. Applying the same biophysical parameters, such as the NDVI for different crop types in the model, may result in large uncertainties in LE estimates.

When the TD-TSEB model is applied for other applications, such as water resources assessment over more complex and heterogeneous basins, two highly effective ways are recommended to reduce uncertainty in LE estimation. First, the easiest approach is to use the LST variation (T_s-LST_0) (LST_0 refers to LST for water bodies or regions of full vegetation cover) to replace the temperature difference (T_s-T_a) to calculate H_s and LE_s. This strategy circumvents the difficulty of calculating T_a from satellite data [*Jiang and Islam*, 2001; *Wang et al.*, 2006; *Tang et al.*, 2010; *Zhang et al.*, 2005; *Zhuang and Wu*, 2015] and reduces 10–15% errors for instantaneous LE_s estimation. Second, the approach is to calibrate and adjust PT coefficient (a), k_{ns}, k_{par}, $NDVI_{min}$, and $NDVI_{max}$ using the ground observations at different vegetation types and climatic zones, which will reduce LE estimation errors by 5–25% [*Anderson et al.*, 2008]. Our next step is produce daily LE product for regional irrigation application using new data fusion techniques, such as the Spatial Temporal Adaptive

Reflectance Fusion Model developed by *Gao et al.* [2006], which integrates daily LE information at moderate resolution from Moderate Resolution Imaging Spectroradiometer with periodic high-resolution LE maps from Landsat.

5.3. Model Advantages and Limitations

Compared to other complex OSEB and TSEB models, the TD-TSEB model has the four advantages. First, it requires relatively fewer inputs (R_s, albedo, LST, T_a, and NDVI) and avoids requiring u to improve the operability of mapping field surface fluxes. Reliable u measurements, which are necessary for calculating aerodynamic resistance, are not routinely available at large scales [*Chen et al.*, 2014; *McVicar et al.*, 2012; *Roderick et al.*, 2007]. Second, the model accounts for intercanopy soil evaporation and undercanopy soil evaporation simultaneously by combining the layer model and the patch model. Third, TD-TSEB is reliable and robust based on the model sensitivity. The sensitivity of the model to the R_s is highest, followed by NDVI, T_a, LST, and albedo, all of which are easily acquired with reasonable accuracy [*Liaqat and Choi*, 2015; *Liu et al.*, 2012]. Finally and fourth, this model circumvents the complex parameterization for aerodynamic and surface resistance involved in OSEB and TSEB models and therefore reduces the accumulated errors from the required forcing data, which produces comparable accuracy of LE estimation when compared with two other widely used surface energy balance models.

Like other TSEB models, the TD-TSEB model also has distinct limitations. First, it is sensitive to its use of the temperature difference (T_s-T_a) to estimate H_s, and the errors in both T_s and T_a reduce the accuracy of H_s and LE_s estimation. Development of the linear relationship between the temperature difference and LST may be a viable method to overcome this limitation in the near future [*Allen et al.*, 2007; *Baik and Choi*, 2015]. Second, TD-TSEB ignores the effects of advection on the partitioning of turbulent energy fluxes because of its assumption of the residual of a surface energy budget that excludes the advection of surface fluxes from the surrounding landscape [*Gowda et al.*, 2008], which may cause large biases in H and LE estimates under strongly advective environment. Our ongoing work will focus on development of the hybrid models by combination of Penman-Monteith model and water balance equation to overcome this disadvantage. Third, the LST separation method proposed by *Lhomme et al.* [1994] used in this study may not accurately calculate surface component temperatures across diverse crop types because this method was originally designed for sparse millet. The error in T_s when this method is applied to other dense crops remains unclear. Perhaps, the use of nonlinear LST separation method would be able to more accurately depict reality. This will be discussed in the near future and is beyond the scope of this study. Finally, the theoretical assumption of a simple inversely proportional relationship between T_s (T_a) and u based on statistical analysis applied to simplify the aerodynamic resistance may be problematic. Considering that the formation of u results from a pressure gradient and temperature difference, the complex functional relationship between temperature, u, and pressure remains unclear [*Kittaka and Miyazaki*, 2014; *Wooten*, 2011]. Such simplification of aerodynamic resistance may weaken the performance of the model. The physical and mathematical linkages between the u and the corresponding temperature require further investigation. Addressing these issues forms the foundation of our ongoing work.

6. Conclusion

We developed a simple temperature domain two-source (TD-TSEB) model by combining the residual of the energy balance equation and a modified PT model. The residual of the energy balance equation is used to estimate LE_s using a temperature domain method based on a simplified framework of total aerodynamic resistances, and a modified PT model is used to estimate LE_c. This model simultaneously accounts for both the intercanopy soil evaporation and undercanopy soil evaporation by combining the "layer" model and the "patch" model. It simplifies the complex parameterization of aerodynamic and surface resistance involved in OSEB and TSEB models to improve the accuracy of LE estimation.

A series of validations conducted at five EC flux tower sites in China and 69 scenes of Landsat TM/ETM+ data indicate that the TD-TSEB model performed well. Sensitivity analysis suggests that the TD-TSEB model is most sensitive to both R_s and NDVI, followed by the T_a, LST, and albedo, all of which are easily acquired with reasonable accuracy. When compared with N95-TSEB and METRIC, the TD-TSEB model has comparable accuracy with fewer inputs. The results of this study are of significant interest for application to other agricultural

regions elsewhere in the world especially in better understanding crop water stress and irrigation, which is important for guiding farmer management practices. This research provides a method to reduce the uncertainty in aerodynamic resistance calculations in data-sparse regions by using appropriate spatial resolution thermal remote sensing data for implementation and evaluation.

Acknowledgments

Authors thank the three anonymous reviewers for their critical and helpful comments and suggestions. Authors also thank both Martha C. Anderson and William P. Kustas from USDA-ARS Hydrology and Remote Sensing Laboratory, Beltsville, Maryland, USA, for their helpful comments and suggestions to improve this manuscript. Authors would also like to thank Zhongli Zhu and Ziwei Xu from School of Geography, Beijing Normal University, China, for providing the metadata of the flux observation data. Flux observation data at Miyun, Daxing, Guantao, and Huailai sites were downloaded from Haihe-Flux (http://westdc.westgis.ac.cn/haihe/), and flux observation data at Daman site were downloaded from HiWATER-MUSOEXE (http://westdc.westgis.ac.cn/hiwater/) under the fair-use policy. Landsat data were downloaded from the Global Visualization Viewer webpage of the USGS (United States Geological Survey) (http://glovis.usgs.gov/). This work was partially supported by the Natural Science Fund of China (41671331 and 41301457) and the National Key Research and Development Program of China (2016YFA0600102 and 2016YFB0501404).

References

Agam, N., S. R. Evett, J. A. Tolk, W. P. Kustas, P. D. Colaizzi, J. G. Alfieri, L. G. McKee, K. S. Copeland, T. A. Howell, and J. L. Chávez (2012), Evaporative loss from irrigated inter rows in a highly advective semi-arid agricultural area, *Adv. Water Resour.*, *50*, 20–30.

Allen, R. G., M. Tasumi, and R. Trezza (2007), Satellite-based energy balance for mapping evapotranspiration with internalized calibration (METRIC) model, *J. Irrig. Drain. Eng.*, *133*(4), 380–394.

Anderson, M. C., J. M. Norman, G. R. Diak, W. P. Kustas, and J. R. Mecikalski (1997), A two-source time-integrated model for estimating surface fluxes using thermal infrared remote sensing, *Remote Sens. Environ.*, *60*(2), 195–216.

Anderson, M. C., J. M. Norman, J. R. Mecikalski, J. A. Otkin, and W. P. Kustas (2007), A climatological study of evapotranspiration and moisture stress across the continental United States based on thermal remote sensing: 1. Model formulation, *J. Geophys. Res.*, *112*, D10117, doi:10.1029/2006JD007506.

Anderson, M. C., J. M. Norman, W. P. Kustas, R. Houborg, P. J. Starks, and N. Agam (2008), A thermal-based remote sensing technique for routine mapping of land-surface carbon, water and energy fluxes from field to regional scales, *Remote Sens. Environ.*, *112*, 4227–4241.

Baik, J., and M. Choi (2015), Evaluation of geostationary satellite (COMS) based Priestley-Taylor evapotranspiration, *Agr. Water Manage.*, *159*, 77–91.

Bastiaanssen, W. G. M., M. Menenti, R. A. Feddes, and A. A. M. Holtslag (1998), A remote sensing surface energy balance algorithm for land (SEBAL): 1. Formulation, *J. Hydrol.*, *212-213*(1–4), 198–212.

Bertoldi, G., J. Albertson, W. Kustas, F. Li, and M. Anderson (2007), On the opposing roles of air temperature and wind speed variability in flux estimation from remotely sensed land surface states, *Water Resour. Res.*, *43*, W10433, doi:10.1029/2007WR005911.

Boegh, E., H. Soegaard, and A. Thomsen (2002), Evaluating evapotranspiration rates and surface conditions using Landsat TM to estimate atmospheric resistance and surface resistance, *Remote Sens. Environ.*, *79*, 329–343.

Brutsaert, W., and M. Sugita (1992), Application of self-preservation in the diurnal evolution of the surface energy budget to determine daily evaporation, *J. Geophys. Res.*, *97*, 18,377–18,382, doi:10.1029/92JD00255.

Carlson, T., and D. Ripley (1997), On the relation between NDVI, fractional vegetation cover, and leaf area index, *Remote Sens. Environ.*, *62*, 241–252.

Chen, T., T. R. McVicar, G. Wang, X. Chen, R. A. M. de Jeu, Y. Y. Liu, H. Shen, F. Zhang, and A. J. Dolman (2016), Advantages of using microwave satellite soil moisture over gridded precipitation products and land surface model output in assessing regional vegetation water availability and growth dynamics for a lateral inflow receiving landscape, *Remote Sens.*, *8*, 428, doi:10.3390/rs8050428.

Chen, Y., et al. (2014), Comparison of satellite-based evapotranspiration models over terrestrial ecosystems in China, *Remote Sens. Environ.*, *140*, 279–293.

Choi, M., W. Kustas, M. Anderson, R. Allen, F. Li, and J. Kjaersgaard (2009), An intercomparison of three remote sensing-based surface energy balance algorithms over a corn and soybean production region (Iowa, U.S.) during SMACEX, *Agric. For. Meteorol.*, *149*, 2082–2097.

Choudhury, B. J., and N. E. DiGirolamo (1998), A biophysical process-based estimate of global land surface evaporation using satellite and ancillary data I. Model description and comparison with observations, *J. Hydrol.*, *205*, 164–185.

Choudhury, B., and J. Monteith (1988), A four-layer model for the heat budget of homogeneous land surfaces, *Q. J. R. Meteorol. Soc.*, *114*, 373–398.

Choudhury, B. J., S. B. Idso, and R. J. Reginato (1987), Analysis of an empirical model for soil heat flux under a growing wheat crop for estimating evaporation by an infrared-temperature-based energy balance equation, *Agric. For. Meteorol.*, *39*, 283–297.

Craig, H., and L. I. Gordon (1965), Deuterium and oxygen 18 variations in the ocean and the marine atmosphere, in *Stable Isotopes in Oceanographic Studies and Paleotemperatures*, edited by E. Tongiorgi, pp. 9–130, Laboratorio di Geologia Nucleare, Pisa.

Dawson, T. E., S. S. O. Burgess, K. P. Tu, R. S. Oliveira, L. S. Santiago, J. B. Fisher, K. A. Simonin, and A. R. Ambrose (2007), Nighttime transpiration in woody plants from contrasting ecosystems, *Tree Physiol.*, *27*, 561–575.

De Bruin, H., and J. Stricker (2000), Evaporation of grass under non-restricted soil moisture conditions, *Hydrol. Sci. J.*, *45*, 391–406.

Denmead, O. T., F. X. Dunin, R. Leuning, and M. R. Raupach (1996), Measuring and modelling soil evaporation in wheat crops, *Phys. Chem. Earth.*, *21*, 97–100.

Dolman, A. J. (1993), A multiple-source land surface energy balance model for use in general circulation models, *Agric. For. Meteorol.*, *65*, 21–45.

Donohue, R. J., M. L. Roderick, T. M. McVicar, and G. D. Farquhar (2013), Impact of CO_2 fertilization on maximum foliage cover across the globe's warm, arid environments, *Geophys. Res. Lett.*, *40*, 3031–3035, doi:10.1002/grl.50563.

Edinger, J. E., D. W. Duttweiller, and J. C. Geyer (1968), The response of water temperature to meteorological conditions, *Water Resour. Res.*, *4*, 1137–1143, doi:10.1029/WR004i005p01137.

Eichinger, W. E., M. B. Parlange, and H. Stricker (1996), On the concept of equilibrium evaporation and the value of the Priestley-Taylor coefficient, *Water Resour. Res.*, *32*, 161–164, doi:10.1029/95WR02920.

Ershadi, A., M. F. McCabe, J. P. Evans, N. W. Chaney, and E. F. Wood (2014), Multi-site evaluation of terrestrial evaporation models using FLUXNET data, *Agric. For. Meteorol.*, *187*, 46–61.

Finnigan, J. J., R. Clement, Y. Malhi, R. Leuning, and H. A. Cleugh (2003), A re-evaluation of long-term flux measurement techniques: Part I. Averaging and coordinate rotation, *Boundary Layer Meteorol.*, *107*, 1–48.

Fisher, J., K. Tu, and D. Baldocchi (2008), Global estimates of the land atmosphere water flux based on monthly AVHRR and ISLSCP-II data, validated at 16 FLUXNET sites, *Remote Sens. Environ.*, *112*, 901–919.

Foken, T. (2008), The energy balance closure problem: An overview, *Ecol. Appl.*, *18*, 1351–1367.

French, A. N., D. J. Hunsaker, and K. R. Thorp (2015), Remote sensing of evapotranspiration over cotton using the TSEB and METRIC energy balance models, *Remote Sens. Environ.*, *158*, 281–294.

Gao, F., J. Masek, M. Schwaller, and F. Hall (2006), On the blending of the Landsat and MODIS surface reflectance: Predicting daily Landsat surface reflectance, *IEEE Trans. Geosci. Remote Sens.*, *44*, 2207–2218.

Gillies, R. R., and T. N. Carlson (1995), Thermal remote-sensing of surface soil-water content with partial vegetation cover for incorporation into climate models, *J. Appl. Meteor.*, *34*, 745–756.
Gowda, P. H., J. L. Chavez, P. D. Colaizzi, S. R. Evett, T. A. Howell, and J. A. Tolk (2008), ET mapping for agricultural water management: Present status and challenges, *Irrigation Sci.*, *26*, 223–237.
Granier, A., and N. Breda (1996), Modelling canopy conductance and stand transpiration of an oak forest from sap flow measurements, *Ann. Forest Sci.*, *53*, 537–546.
Hu, Z. M., X. Wen, X. Sun, L. Li, G. Yu, X. Lee, and S. Li (2014), Partitioning of evapotranspiration through oxygen isotopic measurements of water pools and fluxes in a temperate grassland, *J. Geophys. Res. Biogeosci.*, *119*, 358–372, doi:10.1002/2013JG002367.
Huang, L. J., and X. F. Wen (2014), Temporal variations of atmospheric water vapor δD and $\delta^{18}O$ above an arid artificial oasis cropland in the Heihe River basin, *J. Geophys. Res. Atmos.*, *119*, 11,456–11,476, doi:10.1002/2014JD021891.
Hui, D., S. Wan, B. Su, G. Katul, R. Monson, and Y. Luo (2004), Gap-filling missing data in eddy covariance measurements using multiple imputation (MI) for annual estimations, *Agric. For. Meteorol.*, *121*, 93–111.
Hwang, Y., and M. Choi (2013), Seasonal trends of satellite-based evapotranspiration algorithms over a complex ecosystem in East Asia, *Remote Sens. Environ.*, *137*, 244–263.
Impens, I., and R. Lemur (1969), Extinction of net radiation in different crop canopies, *Theor. Appl. Climatol.*, *17*, 403–412.
Jiang, L., and S. Islam (2001), Estimation of surface evaporation map over Southern Great Plains using remote sensing data, *Water Resour. Res.*, *37*, 329–340, doi:10.1029/2000WR900255.
Jia, Z., S. Liu, Z. Xu, Y. Chen, and M. J. Zhu (2012), Validation of remotely sensed evapotranspiration over the Hai River basin, China, *J. Geophys. Res.*, *117*, D13113, doi:10.1029/2011JD017037.
Jones, H. G. (1992), *Plants and Microclimate: A Quantitative Approach to Environmental Plant Physiology*, 323 pp., Cambridge Univ. Press, Cambridge, U. K.
Jung, M., et al. (2010), Recent decline in the global land evapotranspiration trend due to limited moisture supply, *Nature*, *467*, 951–954.
Kittaka, K., and H. Miyazaki (2014), Relationship between wind direction and air temperature in the Osaka center city determined using fixed point observation, *J. Heat Island Instit. Intern.*, *9-2*, 1–5.
Kalma, J., T. R. McVicar, and M. F. McCabe (2008), Estimating land surface evaporation: A review of methods using remotely sensed surface temperature data accomplished, *Surv. Geophys.*, *29*, 421–469.
Kang, E., G. Cheng, K. Song, B. Jin, X. Liu, and J. Wang (2005), Simulation of energy and water balance in soil-vegetation-atmosphere transfer system in the mountain area of Heihe River basin at Hexi corridor of northwest China, *Sci. China, Ser. D: Earth Sci.*, *48*, 538–548.
Kim, C. P., and D. Entekhabi (1997), Examination of two methods for estimating regional evaporation using a coupled mixed layer and land surface model, *Water Resour. Res.*, *33*, 2109–2116, doi:10.1029/97WR01564.
Kondo, J. (2000) *Atmospheric Science Near the Ground Surface*, pp. 82–84, Univ. of Tokyo Press, Tokyo.
Kool, D., N. Agam, N. Lazarovitch, J. L. Heitman, T. J. Sauer, and A. Ben-Gal (2014), A review of approaches for evapotranspiration partitioning, *Agric. For. Meteorol.*, *184*, 56–70.
Kustas, W., and M. Anderson (2009), Advances in thermal infrared remote sensing for land surface modeling, *Agric. For. Meteorol.*, *149*, 2071–2081.
Kustas, W. P., and J. M. Norman (1997), A two-source approach for estimating turbulent fluxes using multiple angle thermal infrared observations, *Water Resour. Res.*, *33*, 1495–1508, doi:10.1029/97WR00704.
Kustas, W. P., and J. M. Norman (1999), Evaluation of soil and vegetation heat flux predictions using a simple two-source model with radiometric temperatures for partial canopy cover, *Agric. For. Meteorol.*, *94*, 13–29.
Kustas, W. P., Z. Zhang, and T. J. Schmugge (1998), Combining optical and microwave remote sensing for mapping energy fluxes in a semiarid watershed, *Remote Sens. Environ.*, *64*, 116–131.
Kustas, W. P., A. N. French, J. L. Hatefield, T. J. Jackson, S. M. Moran, A. Rango, J. E. Ritchie, and T. J. Schmugge (2003), Remote sensing research in hydrometeorology, *Photogramm. Eng. Rem. S.*, *69*, 613–646.
Lascano, R. J. (2000), A general system to measure and calculate daily crop water use, *Agron. J.*, *92*, 821–832.
Lhomme, J. P., and A. Chehbouni (1999), Comments on dual-source vegetation-atmosphere transfer models, *Agric. For. Meteorol.*, *94*, 269–273.
Lhomme, J. P., and E. Elguero (1999), Examination of evaporative fraction diurnal behaviour using a soil-vegetation model coupled with a mixed-layer model, *Hydrol. Earth Syst. Sci.*, *3*, 259–270.
Lhomme, J. P., B. Monteny, and M. Amadou (1994), Estimating sensible heat flux from radiometric temperature over sparse millet, *Agric. For. Meteorol.*, *68*, 77–91.
Liaqat, U. W., and M. Choi (2015), Surface energy fluxes in the Northeast Asia ecosystem: SEBS and METRIC models using Landsat satellite images, *Agric. For. Meteorol.*, *214-215*, 60–79.
Liang, S. (2000), Narrowband to broadband conversions of land surface albedo. I. Algorithms, *Remote Sens. Environ.*, *76*, 213–238.
Liang, S., K. Wang, X. Zhang, and M. Wild (2010), Review on estimation of land surface radiation and energy budgets from ground measurements, remote sensing and model simulations, *IEEE J. Selec. Top. Appl. Earth Obs. Remote Sens.*, *3*(3), 225–240.
Liu, S., Z. Xu, W. Wang, Z. Jia, M. Zhu, J. Bai, and J. Wang (2011), A comparison of eddy-covariance and large aperture scintillometer measurements with respect to the energy balance closure problem, *Hydrol. Earth Syst. Sci.*, *15*, 1291–1306.
Liu, S., Z. Xu, Z. Zhu, Z. Jia, and M. Zhu (2013), Measurements of evapotranspiration from eddy-covariance systems and large aperture scintillometers in the Hai River basin, China, *J. Hydrol.*, *487*, 24–38.
Liu, Y., T. Hiyama, T. Yasunari, and H. Tanaka (2012), A nonparametric approach to estimating terrestrial evaporation: Validation in eddy covariance sites, *Agric. For. Meteorol.*, *157*, 49–59.
Li, X., et al. (2013), Heihe watershed allied telemetry experimental research (HiWATER): Scientific objectives and experimental design, *Bull. Amer. Meteor. Soc.*, *94*, 1145–1160.
Long, D., and V. P. Singh (2012), A two-source trapezoid model for evapotranspiration (TTME) from satellite imagery, *Remote Sens. Environ.*, *121*, 370–388.
Long, D., and V. P. Singh (2013), Assessing the impact of end-member selection on the accuracy of satellite-based spatial variability models for actual evapotranspiration estimation, *Water Resour. Res.*, *49*, 2601–2618, doi:10.1002/wrcr.20208.
Mahrt, L. (2010), Computing turbulent fluxes near the surface: Needed improvements, *Agric. For. Meteorol.*, *150*, 501–509.
Matsumoto, K., T. Ohta, and T. Tanaka (2005), Dependence of stomatal conductance on leaf chlorophyll concentration and meteorological variables, *Agric. For. Meteorol.*, *132*, 44–57.
McVicar, T. R., and D. L. P. Jupp (1999), Estimating one-time-of-day meteorological data from standard daily data as inputs to thermal remote sensing based energy balance models, *Agric. For. Meteorol.*, *96*, 219–238.

McVicar, T. R., and D. L. B. Jupp (2002), Using covariates to spatially interpolate moisture availability in the Murray-Darling Basin: A novel use of remotely sensed data, *Remote Sens. Environ.*, *79*, 199–212.
McVicar, T., et al. (2012), Global review and synthesis of trends in observed terrestrial near-surface wind speeds: Implications for evaporation, *J. Hydrol.*, *416-417*, 182–205.
Mu, Q., F. A. Heinsch, M. Zhao, and S. W. Running (2007), Development of a global evapotranspiration algorithm based on MODIS and global meteorology data, *Remote Sens. Environ.*, *111*(4), 519–536.
Mu, Q., M. Zhao, and S. W. Running (2011), Improvements to a MODIS global terrestrial evapotranspiration algorithm, *Remote Sens. Environ.*, *115*(8), 1781–1800.
Nishida, K., R. R. Nemani, S. W. Running, and J. M. Glassy (2003), An operational remote sensing algorithm of land surface evaporation, *J. Geophys. Res.*, *108(*D9*)*, 4270, doi:10.1029/2002JD002062.
Norman, J. M., W. P. Kustas, and K. S. Humes (1995), A two-source approach for estimating soil and vegetation energy fluxes from observations of directional radiometric surface temperature, *Agric. For. Meteorol.*, *77*, 263–293.
Norman, J. M., W. P. Kustas, J. H. Prueger, and G. R. Diak (2000), Surface flux estimation using radiometric temperature: A dual-temperature-difference method to minimize measurement errors, *Water Resour. Res.*, *36*, 2263–2274, doi:10.1029/2000WR900033.
Norman, J. M., M. C. Anderson, W. P. Kustas, A. N. French, J. Mecikalski, R. Torn, G. R. Diak, T. J. Schmugge, and B. C. W. Tanner (2003), Remote sensing of surface energy fluxes at 101-m pixel resolutions, *Water Resour. Res.*, *39*(8), 1221, doi:10.1029/2002WR001775.
Potter, C. S., et al. (1993), Terrestrial ecosystem production: A process model based on global satellite and surface data, *Global Biogeochem. Cycles*, *7*, 811–841, doi:10.1029/93GB02725.
Priestley, C. H. B., and R. J. Taylor (1972), On the assessment of surface heat flux and evaporation using large-scale parameters, *Mon. Weather Rev.*, *100*(2), 81–92.
Qin, Z., A. Karnieli, and P. Berliner (2001), A mono-window algorithm for retrieving land surface temperature from Landsat TM data and its application to the Israel-Egypt border region, *Int. J. Remote Sens.*, *22*, 3719–3746.
Qiu, G., P. Shi, and L. Wang (2006), Theoretical analysis of a remotely measurable soil evaporation transfer coefficient, *Remote Sens. Environ.*, *101*, 390–398.
Roderick, M. L., L. D. Rotstayn, G. D. Farquhar, and M. T. Hobbins (2007), On the attribution of changing pan evaporation, *Geophys. Res. Lett.*, *34*, L17403, doi:10.1029/2007GL031166.
Ross, J. (1976), Radiative transfer in plant communities, in *Vegetation and the Atmosphere*, edited by J. L. Monteith, pp. 13–56, Academic Press, London.
Ruimy, A., L. Kergoat, and A. Bondeau (1999), Comparing global models of terrestrial net primary productivity (NPP): Analysis of differences in light absorption and light-use efficiency, *Global Change Biol.*, *5*, 56–64.
Sánchez, J. M., W. P. Kustas, V. Sánchez, and M. C. Anderson (2008), Modelling surface energy fluxes over maize using a two-source patch model and radiometric soil and canopy temperature observations, *Remote Sens. Environ.*, *112*, 1130–1143.
Sauer, T. J., J. M. Norman, C. B. Tanner, and T. B. Wilson (1995), Measurement of heat and vapor transfer coefficients at the soil surface beneath a maize canopy using source plates, *Agric. For. Meteorol.*, *75*, 161–189.
Schlesinger, W. H., and S. Jasechko (2014), Transpiration in the global water cycle, *Agric. For. Meteorol.*, *189-190*, 115–117.
Schmid, H. P. (1997), Experimental design for flux measurements: Matching scales of observations and fluxes, *Agric. For. Meteorol.*, *87*, 179–200.
Seguin, B., and B. Itier (1983), Using midday surface temperatures to estimate daily evaporation from satellite thermal IR data, *Int. J. Remote Sens.*, *4*, 371–383.
Singer, J. W., et al. (2010), Contrasting methods for estimating evapotranspiration in soybean, *Agr. Water Manage.*, *98*, 157–163.
Song, L., et al. (2016), Application of remote sensing-based two-source energy balance model for mapping field surface fluxes with composite and component surface temperatures, *Agric. For. Meteorol.*, *230-231*, 8–19.
Stewart, J. B., W. P. Kustas, K. S. Humes, W. D. Nichols, M. S. Moran, and H. A. R. de Bruin (1994), Sensible heat flux-radiometric surface temperature relationships for eight semi-arid areas, *J. Appl. Meteorol.*, *33*, 1110–1117.
Sugita, M., and W. Brutsaert (1991), Daily evaporation over a region from lower boundary layer profiles measured with radiosondes, *Water Resour. Res.*, *27*, 747–752, doi:10.1029/90WR02706.
Sun, J., and L. Mahrt (1995), Determination of surface fluxes from the surface radiative temperature, *J. Atmos. Sci.*, *52*, 1096–1106.
Sun, J. L., W. Massman, and D. A. Grantz (1999), Aerodynamic variables in the bulk formulation of turbulent fluxes, *Bound. -Layer Meteor.*, *91*, 109–125.
Su, Z. (2002), The Surface Energy Balance System (SEBS) for estimation of turbulent heat fluxes, *Hydrol. Earth Syst. Sci.*, *6*, 85–100.
Tang, R., Z. Li, and B. Tang (2010), An application of the Ts-VI triangle method with enhanced edges determination for evapotranspiration estimation from MODIS data in arid and semi-arid regions: Implementation and validation, *Remote Sens. Environ.*, *114*, 540–551.
Tasumi, M. (2003), Progress in operational estimation of regional evapotranspiration using satellite imagery, PhD dissertation, pp. 351–357, Univ. of Idaho, Moscow, Id.
Tasumi, M., R. G. Allen, and R. Trezza (2008), At-surface reflectance and albedo from satellite for operational calculation of land surface energy balance, *J. Hydrol. Eng.*, *13*, 51–63.
Thom, A. S. (1975), *Momentum, Mass and Heat Exchange of Plant Communities*, edited by J. L. Monteith, pp. 57–109, Vegetation and the Atmosphere Academic Press, London.
Tucker, C. J. (1979), Red and photographic infrared linear combinations for monitoring, *Remote Sens. Environ.*, *8*, 127–150.
Twine, T. E., W. P. Kustas, J. M. Norman, D. R. Cook, P. R. Houser, T. P. Meyers, J. H. Prueger, P. J. Starks, and M. L. Wesely (2000), Correcting eddy-covariance flux underestimates over a grassland, *Agric. For. Meteorol.*, *103*, 279–300.
Van Niel, T. G., T. R. McVicar, M. L. Roderick, A. I. J. M. van Dijk, L. J. Renzullo, and E. van Gorsel (2011), Correcting for systematic error in satellite-derived latent heat flux due to assumptions in temporal scaling: Assessment from flux tower observations, *J. Hydrol.*, *409*, 140–148.
Van Niel, T. G., T. R. McVicar, M. L. Roderick, A. I. J. M. van Dijk, J. Beringer, L. B. Hutley, and E. van Gorsel (2012), Upscaling latent heat flux for thermal remote sensing studies: Comparison of alternative approaches and correction of bias, *J. Hydrol.*, *468-469*, 35–46.
Verhoef, A., H. A. R. De Bruin, and B. J. J. M. Van Den Hurk (1997), Some practical notes on the parameter kB^{-1} for sparse vegetation, *J. Appl. Meteorol.*, *36*, 560–572.
Wallace, J. S., and C. J. Holwill (1997), Soil evaporation from Tiger-bush in south-west Niger, *J. Hydrol.*, *188–189*, 426–442.
Wang, K., and R. Dickinson (2012), A review of global terrestrial evapotranspiration: Observation, modeling, climatology and climatic variability, *Rev. Geophys.*, *50*, RG2005, doi:10.1029/2011RG000373.
Wang, K., Z. Li, and M. Cribb (2006), Estimation of evaporative fraction from a combination of day and night land surface temperatures and NDVI: A new method to determine the Priestley-Taylor parameter, *Remote Sens. Environ.*, *102*, 293–305.

Wen, X. F., et al. (2012), Dew water isotopic ratios and their relationships to ecosystem water pools and fluxes in a cropland and a grassland in China, *Oecologia*, *168*, 549–561.
Wen, X. F., B. Yang, X. M. Sun, and X. H. Lee (2016), Evapotranspiration partitioning through in-situ oxygen isotope measurements in an oasis cropland, *Agric. For. Meteorol.*, *230-231*, 89–96.
Wilson, K., et al. (2002), Energy balance closure at FLUXNET sites, *Agric. For. Meteorol.*, *113*, 223–243.
Wooten, R. D. (2011), Statistical analysis of the relationship between wind speed, pressure and temperature, *J. Appl. Sci.*, *11*, 2712–2722.
World Meteorological Organization, (2008), *Guide to Meteorological Instruments and Methods of Observation*, 7th ed, pp. 1–25, World Meteorol. Organ., Geneva, Switzerland.
Xiong, Y., S. Zhao, F. Tian, and G. Qiu (2015), An evapotranspiration product for arid regions based on the three-temperature model and thermal remote sensing, *J. Hydrol.*, *530*, 392–404.
Xu, Z., et al. (2013), Intercomparison of surface energy flux measurement systems used during the HiWATER-MUSOEXE, *J. Geophys. Res. Atmos.*, *118*, 13,140–13,157, doi:10.1002/2013JD020260.
Yang, C., et al. (2015), Analysis on evapotranspiration of maize field measured by Lysimeters in Huailai, *Plateau Meteorol.*, *34*, 1095–1106 (In Chinese).
Yang, Y., and S. Shang (2013), A hybrid dual-source scheme and trapezoid framework–based evapotranspiration model (HTEM) using satellite images: Algorithm and model test, *J. Geophys. Res. Atmos.*, *118*, 2284–2300, doi:10.1002/jgrd.50259.
Yang, Y., D. Long, and S. Shang (2013), Remote estimation of terrestrial evapotranspiration without using meteorological data, *Geophys. Res. Lett.*, *40*, 3026–3030, doi:10.1002/grl.50450.
Yang, Y., D. Long, H. Guan, W. Liang, C. Simmons, and O. Batelaan (2015), Comparison of three dual-source remote sensing evapotranspiration models during the MUSOEXE-12 campaign: Revisit of model physics, *Water Resour. Res.*, *51*, 3145–3165, doi:10.1002/2014WR015619.
Yan, H., et al. (2012), Global estimation of evapotranspiration using a leaf area index-based surface energy and water balance model, *Remote Sens. Environ.*, *124*, 581–595.
Yao, Y., et al. (2013), MODIS-driven estimation of terrestrial latent heat flux in China based on a modified Priestley-Taylor algorithm, *Agric. For. Meteorol.*, *171-172*, 187–202.
Yao, Y., et al. (2015), A satellite-based hybrid algorithm to determine the Priestley-Taylor parameter for global terrestrial latent heat flux estimation across multiple biomes, *Remote Sens. Environ.*, *165*, 216–233.
Yebra, M., A. Van Dijk, R. Leuning, A. Huete, and J. Guerschman (2013), Evaluation of optical remote sensing to estimate actual evapotranspiration and canopy conductance, *Remote Sens. Environ.*, *129*, 250–261.
Yuan, W. P., et al. (2010), Global estimates of evapotranspiration and gross primary production based on MODIS and global meteorology data, *Remote Sens. Environ.*, *114*, 1416–1431.
Zeggaf, A. T., S. Takeuchi, H. Dehghanisanij, H. Anyoji, and T. Yano (2008), A Bowen ratio technique for partitioning energy fluxes between maize transpiration and soil surface evaporation, *Agron. J.*, *100*, 988–996.
Zhan, X., and W. P. Kustas (2001), A coupled model of land surface CO_2 and energy fluxes using remote sensing data, *Agric. For. Meteorol.*, *107*, 131–152.
Zhan, X., W. P. Kustas, and K. S. Humes (1996), An intercomparison study on models of sensible heat flux over partial canopy surfaces with remotely sensed surface temperature, *Remote Sens. Environ.*, *58*, 242–256.
Zhang, C., W. Zhang, and L. Guo (2013), Relation between variation characteristics and climatic influencing factors of ground temperature in Shijiazhuang in recent 50 years, *Meteorol. Sci. Technol.*, *41*, 558–562 (In Chinese).
Zhang, F. M., J. M. Chen, J. Q. Chen, C. M. Gough, T. A. Martin, and D. Dragoni (2012), Evaluating spatial and temporal patterns of MODIS GPP over the conterminous U.S. against flux measurements and a process model, *Remote Sens. Environ.*, *124*, 717–729.
Zhang, K., J. S. Kimball, Q. Mu, L. Jones, S. Goetz, and S. Running (2009), Satellite based analysis of northern ET trends and associated changes in the regional water balance from 1983 to 2005, *J. Hydrol.*, *379*, 92–110.
Zhang, R. H., X. M. Sun, W. M. Wang, J. P. Xu, Z. L. Zhu, and J. Tian (2005), An operational two-layer remote sensing model to estimate surface flux in regional scale: Physical background, *Sci. China, Ser. D: Earth Sci.*, *48*, 225–244.
Zhang, X., S. Liang, G. Zhou, H. Wu, and X. Zhao (2014), Generating Global LAnd Surface Satellite incident shortwave radiation and photosynthetically active radiation products from multiple satellite data, *Remote Sens. Environ.*, *152*, 318–332.
Zhang, Y., R. Leuning, L. Hutley, J. Beringer, I. McHugh, and J. Walker (2010), Using long-term water balances to parameterize surface conductances and calculate evaporation at 0.05° spatial resolution, *Water Resour. Res.*, *46*, W05512, doi:10.1029/2009WR008716.
Zhuang, Q., and B. Wu (2015), Estimating evapotranspiration from an improved two-source energy balance model using ASTER satellite imagery, *Water*, *7*, 6673–6688.